Electronic Supplementary Material (ESI) for Journal of Materials Chemistry C.

Supporting Information

Heteroatom-Directed Supramolecular Helical-rich Architectures in N-terminal Protected Pyridyl Aromatic Amino Acids

Thangavel Vijayakanth,[†] Bin Xue,[§] Sarah Guerin,[‖] Sigal Rencus-Lazar,[†] Natalia Fridman,[⊥] Damien Thompson,[‖] Yi Cao,[§] Ehud Gazit*,[†,‡]

[†]Shmunis School of Biomedicine and Cancer Research, George S. Wise Faculty of Life Sciences, Tel Aviv University, Tel Aviv – 6997801, Israel.

[‡]Department of Materials Science and Engineering, Iby and Aladar Fleischman Faculty of Engineering, Tel Aviv University, Tel Aviv –6997801, Israel.

[§]National Laboratory of Solid-State Microstructure, Department of Physics, Nanjing University, Nanjing 210000, China.

[‖]Department of Physics, Bernal Institute, University of Limerick, Limerick V94 T9PX, Ireland.

[⊥]Schulich Faculty of Chemistry, Technion-Israel Institute of Technology, Haifa – 32000, Israel.

Table of Contents

EXPERIMENTAL SECTION

1. Materials

The 9-fluorenylmethoxycarbonyl (Fmoc) protected amino acid residues were purchased from Bachem (Bubendorf, Switzerland) and Sigma Aldrich (Rehovot, Israel). Milli-Q purified water was used to prepare the self-assembled structures. All materials were used as received without further purification.

2. Single-crystal Preparation

Single crystals for data collection were obtained at room temperature using a slow evaporation method. The isomers of Fmoc-**L**-PyA and Fmoc-**D**-PyA were dissolved in methanol (MeOH) at a concentration of 10 mg/mL. The dissolved clear solution was then placed in a glass vial and sealed with Parafilm®, which was pierced five times with a needle and allowed to crystallize at room temperature. Colourless needles developed within three days and reached their maximum size after five days.

The racemic mixture of Fmoc-**DL**-PyA crystals were prepared by dissolving the equimolar ratio of Fmoc-**L**-PyA and Fmoc-**D**-PyA in methanol at a concentration of 5 mg/0.5 mL of each. The crystallization technique was then repeated using the same procedure as outline above.

3. Characterization

X-ray Single Crystal Diffraction Analysis. Single-crystal X-ray diffraction analyses of Fmoc-**L**-PyA, Fmoc-**D**-PyA and Fmoc-**DL**-PyA were performed on a Bruker Apex II Duo diffractometer using Mo Kα radiation (λ= 0.71073Å). The crystal structures were solved by using direct methods and then refined by full-matrix least-squares against F^2 using all data by using the SHELXL-2014/7 program package as implemented in Olex2.[1] The crystallographic refinement data for Fmoc-**L**-PyA, Fmoc-**D**-PyA and Fmoc-**DL**-PyA are listed in (Table S1). All the non-hydrogen atoms were refined anisotropically unless stated otherwise. Hydrogen atoms were constructed in geometric positions to their parent atoms.[2] The ORTEP (Oak Ridge Thermal Ellipsoid Plot) program was used to illustrate 50% probability thermal ellipsoids using Mercury software. The DIAMOND-3.1 and Mercury software packages were used to describe the bond length, bond angles and various structural illustrations. Crystallographic data have been deposited at the Cambridge Crystallographic Data Centre (CCDC), with the deposition numbers 2211500 (Fmoc-**L**-PyA), 2211501 (Fmoc-**D**-PyA), 2211502 (Fmoc-**DL**-PyA, **P1**), 2211503 (Fmoc-**DL**-PyA, **P2**).

Circular Dichroism (CD) Spectroscopy. CD spectra of Fmoc-**L**-PyA, Fmoc-**D**-PyA, and Fmoc-**DL**-PyA (1 mg/mL) in MeOH were recorded using a Chirascan spectrometer (Applied Photophysics) fitted with a Peltier temperature controller set to 25 °C, using quartz cuvettes with an optical path length of 0.1 mm (Hellma Analytics). The scan was carried out in 1 nm steps over a wavelength range of 190-260 nm, with a spectral bandwidth of 1.0 nm and a 3 s average period. The full spectrum of the sample was collected three times and averaged. A MeOH, a baseline was recorded and subtracted from the sample spectra in the same manner. The Pro-Data Viewer software (Applied Photophysics) was used to process the data.

Fourier Transform Infrared Spectroscopy (FT-IR). The enantiomers and the racemic mixture were dissolved in MeOH at a concentration of 10 mg/ml. The solution was concentrated up to approximately 50 µL and was deposited on disposable potassium bromide (KBr) infrared sample cards (Sigma-Aldrich) and dried at room temperature for a day. The spectral data were collected using a Nicolet Nexus 470 FTIR spectrometer with a deuterated triglycine sulfate (TGS) detector. The absorbance maxima values were determined using an OMNIC analysis program. The experiments were performed at a resolution of 8 cm^{-1} and an average of 64 scans in the 400 to 4000 cm^{-1} spectral range. The spectral data were extracted after subtracting the background.

Raman Spectroscopy. The Raman active modes of the powdered samples of enantiomers and the conjugate mixtures were recorded using Raman spectroscopy (λ_{exc} = 532 nm) with a LabRAM HR, Horbia Jobin Yvon microscope model and 50X objective lens. The entire spectra ranging from 100-4000 cm^{-1} were recorded.

Ultra-violet Spectroscopy. The Fmoc-protected chiral amino acids and the racemic mixtures were dissolved in methanol (MeOH) at a concentration of 0.5 mg/ml. A 50 µL aliquot was pipetted out from the solution and diluted with 950 µL MeOH. The UV spectra were recorded using Cary series UV-Vis Spectrophotometer (Agilent Technologies). The spectral data were extracted after subtracting the MeOH background.

Hirshfeld Surface Analysis. The Crystal Explorer 3.1 program was used to perform Hirshfeld surface mapping of all non-covalent molecular interactions of Fmoc-**L**-PyA, Fmoc-**D**-PyA and Fmoc-**DL**-PyA (**P1**).[3] To display all types of interactions that exist on the Hirshfeld surface, the single-crystal X-ray crystallographic information file (CIF) was used. The normalized contact distance (dnorm), shape index, and curvedness of these interactions were acquired as 3D colour mapping images. Surface colour mappings were generated on the Hirshfeld surface by colour coding based on strong (red), medium (blue) and weak (white) interactions. The shape index indicates the local shape of the concave and convex regions based on the features of the Hirshfeld surface. The maximum and the selected range of the surface index were used between 1.0 and -1.0 which corresponds to the most convex and concave regions. For the minimal surface regions, these values were fixed to 0. Curvedness denotes a measure of how much the shape can get curved from the Hirshfeld surface which has a general useful range of -4.0 to 0.4. The 2D fingerprint plot of Fmoc-**L**-PyA, Fmoc-**D**-PyA and Fmoc-**DL**-PyA (**P1**) could be constructed by the distance of an atom that is nearest to the interior (di) and exterior (de) of the generated Hirshfeld surface. Based on the Hirshfeld surface, the different contours (blue and grey colour) contained in the 2D fingerprint plot explain the many types of chemical interactions, as well as specific and all contact information. The surface generation of the Hirshfeld images was constructed with an iso-value of a weight function of 0.5 au. The observed Hirshfeld analysis data of Fmoc-**L**-PyA, Fmoc-**D**-PyA and Fmoc-**DL**-PyA (**P1**) are summarized in Table S9.

Powder X-ray Diffraction. Crystal powder diffraction patterns were obtained using a D8 Advance X-ray diffractometer (Bruker, Germany) equipped with a linear LYNXEYE XE detector. The data was collected between the 2θ range of 3 to 40°. The diffraction peaks were extracted after subtracting the background.

Thermogravimetric Analysis (TGA). TGA measurements were performed using a TA Instruments (USA) module TGA 2950, at a temperature range between 313 K and 873 K with a temperature interval of 10 K min^{-1}, under a dry ultrahigh-purity argon atmosphere.

Scanning Electron Microscopy (SEM). For the self-assembly process, amino acid stock solutions were prepared at a concentration of 1 mg/mL in different solvents: 100% methanol (MeOH), 90:10% MeOH/water (H_2O), and 95:5% dimethyl sulfoxide (DMSO)/H_2O. Enantiomers and their racemic mixtures completely dissolved in MeOH and in DMSO. Upon the addition of H_2O to the MeOH or DMSO, self-assembled aggregates were observed. In all cases, a 20 µL aliquot of the prepared stock sample was dried at room temperature on a microscope coverslip and a Quorum SC7620 sputter coater system was used to sputter gold on the self-assembled samples at 15 mA for 45 seconds to improve the conductivity of the sample surface. SEM images were obtained using Zeiss Gemini 300 (Zeiss, Germany) with an operating voltage range from 1 to 3 kV.

Young’s Modulus Measurement. Atomic force microscopy (AFM) nanoindentation experiments were performed using a commercial AFM (JPK, Nanowizard IV, Berlin, Germany). The crystals were spread on mica substrates and then blown with nitrogen to remove the loose samples. Typically, the cantilever was moved to the surface of the crystals and performed on the flat area (scan area: 5 μm × 5 μm) at the QI mode (conditions: pixels: 60 × 60; Z length: 0.1 μm; extend and retract speed: 30 μm s^{-1}; Z resolution: 80000 Hz; maximum loading force: 800 nN). RTESPA-525 cantilevers (Bruker Company, half-open angle of the pyramidal face of θ: < 10°, tip radius: ~10 nm, spring constant: ~200 N m^{-1}) were used in all the experiments. Then, the cantilever was extended to the surface of the crystal and retracted while the force and displacement during the process were recorded. Young’s modulus of the crystals could be calculated by fitting the extending curve with the Hertz model (1).

$$F = \frac{4}{3}\frac{E}{(1-v^2)}\sqrt{R}\delta^{3/2} \qquad (1)$$

Where *F* corresponds to the force, *δ* corresponds to the depth of the crystal pressed by the cantilever tip, *R* is the radius of the tip, *E* is Young's modulus of the crystals and *v* is the Poisson ratio ($v = 0.3$). The point stiffness was determined as the normal force divided by the deformation of the sample and calculated from the force-displacement curves after deducting the deformation of the cantilever. For each sample, more than six regions and 1-2 flat areas in each location were randomly selected to perform the nanoindentation. At least two cantilevers were used in the experiments to exclude tip dependency of the results. All the data was analysed and the two-dimensional diagrams were reconstructed using the JPK data processing 7.0.46 software (JPK company).

Computational Details.

Classical piezoelectricity manifests itself in both a direct and a converse effect. The direct piezoelectric effect is a linear coupling between mechanical stress and electrical polarization. The converse piezoelectric effect is a linear coupling between mechanical strain and an applied electric field. Both behaviours are described by the same set of piezoelectric constants, most commonly the piezoelectric strain constant d_{ij}, which is measured in pC/N for the direct piezoelectric effect, and pm/V for the converse piezoelectric effect.

Mathematically, this piezoelectric response can be described by a third rank tensor in the form of a 3 × 6 matrix:

$$\begin{pmatrix} d_{11} & d_{12} & d_{13} & d_{14} & d_{15} & d_{16} \\ d_{21} & d_{22} & d_{23} & d_{24} & d_{25} & d_{26} \\ d_{31} & d_{32} & d_{33} & d_{34} & d_{35} & d_{36} \end{pmatrix} \qquad \text{Equation 1}$$

Here d_{11}, d_{22}, and d_{33} are defined as the longitudinal piezoelectric strain coefficients, with the final three columns containing the shear piezoelectric strain coefficients. The remaining matrix components represent the transverse piezoelectric strain coefficients, defined according to the direction of the applied stimulus and the direction of the resulting response.

Electromechanical properties were predicted from periodic Density Functional Theory (DFT)[4] calculations on single crystals using the VASP[5] code. For a full overview on DFT readers are directed to more thorough overviews[6,7]. A number of multiscale modelling techniques can be used to evaluate and simulate electromechanical properties[8], and within DFT other suitable softwares include CP2K[9], ABINIT[10], and CASTEPl[11].

Electronic structures were calculated using the PBE functional[12] with Grimme-D3 dispersion corrections[13] and projector augmented wave (PAW) pseudopotentials[14]. Calculations were carries out using Gaussian smearing, and a plane wave cut-off of 600 eV. Piezoelectric charge constants, e_{ij}, were calculated using density functional perturbation theory (DFPT)[15]. For this a 2×2×2 Γ-centred *k*-point grid was also used,

The theoretical methodology herewith consists of four steps:

geometry optimisation

calculation of piezoelectric charge tensor

calculation of elastic constants

calculation of static dielectric tensor

Geometry Optimisation

The first step is to take the experimental crystal structures of interest, and allow their lattice parameters and atomic positions to relax in order to obtain ideal ground state structures. Experimental structures were downloaded from the Cambridge Crystallographic Data Centre (CCDC). All crystal structures were optimised using the conjugate gradient algorithm[16]. For a periodic system, integrals in real space over the infinitely extended system are replaced by integrals over the finite first Brillouin zone in reciprocal space, in accordance with Bloch's theorem. These integrals are performed at a finite number of points in the Brillouin zone, called the k-point mesh, or grid. A 4×4×4 Γ-centred *k*-point grid was used for geometry optimisations; with a plane wave energy cut-off of 600 eV (all plane waves with a kinetic energy less than this are included in the basis set). Γ-centred *k*-point grids are generally recommended for non-centrosymmetric unit cells. These values were obtained after energy convergence tests with respect to N (where N = number of subdivisions of the reciprocal lattice vector), and plane wave cut off energy. Minimum converged are chosen to balance calculation accuracy with computational expense.

Elastic Constants

The elastic stiffness constants c_{kj}, are required to calculate the piezoelectric strain constants d_{ik}. The elastic constants are also important experimentally. The elastic compliance can easily be derived from the stiffness and measured using impedance spectroscopy or nanoindentation, as can the Young's Modulus, which is important for device applications. Using the piezoelectric charge coefficients, e_{ij}, which are calculated directly by VASP, and the elastic stiffness constants, c_{kj}, we can calculate the more useful piezoelectric strain coefficient, d_{ik}, using the relationship

$$d_{ik} = {}^{e_{ij}}/_{c_{kj}} \qquad \text{Equation 2}$$

The elastic constants are calculated in the form of the stiffness tensor, ***C***, presented as a 6×6 matrix. VASP outputs this tensor in Voigt notation in kB, so post analysis is required to produce C in matrix notation in GPa.

$$C = \begin{pmatrix} \boldsymbol{c_{11}} & c_{12} & c_{13} & c_{14} & c_{15} & c_{16} \\ c_{21} & \boldsymbol{c_{22}} & c_{23} & c_{24} & c_{25} & c_{26} \\ c_{31} & c_{32} & \boldsymbol{c_{33}} & c_{34} & c_{35} & c_{36} \\ c_{41} & c_{42} & c_{43} & \boldsymbol{c_{44}} & c_{45} & c_{46} \\ c_{51} & c_{52} & c_{53} & c_{54} & \boldsymbol{c_{55}} & c_{56} \\ c_{61} & c_{62} & c_{63} & c_{64} & c_{65} & \boldsymbol{c_{66}} \end{pmatrix} \qquad \text{Equation 3}$$

For this work, it is only necessary to extract the six primary diagonal matrix components, shown in bold in equation 2. The number of non-zero elements in both the elastic and piezoelectric matrices will vary according to the symmetry of the crystal being studied. Young's Moduli were derived from the stiffness and its inverse compliance matrix components. Values are presented as Voigt-Reuss-Hill averages[17,18] as calculated by the ELATE software tool[19]. Crystal structures were visualised using VESTA[20]. Currently, VASP only supports the calculation of the ionic contribution to the elastic stiffness constants using DFPT, and so cannot be used to derive the full elastic stiffness tensor. For more information on these constants, their matrix representations and their units, readers are directed to Nye[21].

Dielectric Tensor

DFPT calculations can also predict the static dielectric tensor of the crystal being studied. Using the dielectric tensor we can extract the final piezoelectric constant: the voltage constant, g_{ik}. This is an important figure of merit (FoM) for energy harvesting applications, and in motion and pressure sensing. To obtain these g_{ik} values we divide the corresponding piezoelectric strain constant, d_{ik}, by the relevant dielectric constant ε_{ii}, as shown in equation 3. These constants are measured in V m/N.

$$g_{ik} = {}^{d_{ik}}\!/\varepsilon_{ii}\ \varepsilon_{o} \qquad \text{Equation 4}$$

The accuracy of the computational methods used in the simulation of permittivity, elastic stiffness, and piezoelectricity, has been extensively benchmarked and validated in previous publications. Initially the methodology was benchmarked with respect to three well-known inorganic piezoelectric materials; namely aluminium nitride (AlN), zinc oxide (ZnO) and α-quartz (SiO_2). This was then extended to the proteinogenic amino acids[22], biominerals[23], co-crystals[24] and peptides[25], with deviations from experiment ranging from 1-20%, which is highly accurate for identifying high-performance materials. The upper limit is observed in highly flexible materials with individual stiffness constants of less than 5 GPa.

Table S1. Crystallographic data for the enantiomers and racemic mixture of Fmoc-PyA.

Compound	Fmoc-**L**-PyA	Fmoc-**D**-PyA	Fmoc-**DL**-PyA **(P1)**	Fmoc-**DL**-PyA **(P2)**
CCDC number	2211500	2211501	2211502	2211503
Chemical formula	$C_{23}H_{20}N_2O_4$	$C_{23}H_{20}N_2O_4$	$C_{23}H_{20}N_2O_4$	$C_{23}H_{20}N_2O_4$
Formula weight (g/mol)	388.41	388.41	388.41	388.41
Temperature (K)	200.15	200.15	140.15	140.15
Crystal system	Orthorhombic	Orthorhombic	Monoclinic	Monoclinic
Space group	$P2_12_12_1$	$P2_12_12_1$	$P2_1/c$	$P2_1/c$
a (Å); α (°)	4.973(5); 90	4.9371(9); 90	25.917(11); 90	12.510(3); 90
b (Å); β (°)	8.157(8); 90	8.0769(15); 90	4.929(2); 97.334(10)	29.996(7); 97.787(7)
c (Å); γ (°)	48.990(5); 90	48.489(9); 90	15.665(7); 90	5.7849(13); 90
V (Å^3); Z	1987(3); 4	1933.6(6); 4	1984.7(15); 4	2150.8(9); 4
Radiation	MoKα (λ = 0.71073)	MoKα (λ = 0.71073)	MoKα (λ = 0.71073)	MoKα (λ = 0.71073)
Computing data_collection	Bruker Instrument Service	Bruker Instrument Service	Bruker Instrument Service	Bruker Instrument Service
Crystal size/mm^3	0.27 × 0.15 × 0.12	0.27 × 0.09 × 0.06	0.27 × 0.12 × 0.09	0.21 × 0.09 × 0.06
Absorption correction method	Multi-scan	Multi-scan	Multi-scan	Multi-scan
ρ (calc.) g cm^{-3}	1.298	1.334	1.300	1.199
μ(Mo K$_α$) mm^{-1}	0.090	0.092	0.090	0.083
2θ$_{max}$ (°)	48.93	48.98	48.83	49.158
R(int)	0.0831	0.0606	0.0950	0.0692
Completeness to θ	98.0	99.5	98.4	97.2
Data/restraints/parameters	2519/268/268	3194/0/263	2155/268/263	3518/737/382
Goodness-of-fit on F^2	1.027	1.092	0.901	1.002
Final R indexes [I>=2σ (I)]	0.0905	0.0491	0.0597	0.0791
Final R indexes [all data]	0.2295	0.1071	0.1541	0.2400
Largest diff. peak/hole / e Å^{-3}	0.29/-0.24	0.18/-0.18	0.17/-0.22	0.23/-0.19

Table S2. Crystallographic data for the enantiomers and racemic mixture of Fmoc-PyA.

Compound	**D-H…A**	**d(D-H) (Å)**	**d(H…A) (Å)**	**d(D-A) (Å)**	**<DHA (º)**	**Symmetry operations**
Fmoc-**L**-PyA	N1-H1…O2	0.8806(1003)	2.3497(994)	3.1069(113)	144.191(8584)	x, -2+y, 1+z
200.15 K	O4-H4…N2	0.8393(62)	1.7585(74)	2.5843(97)	167.508(487)	-x, -1.5+y, -0.5-z
Fmoc-**D**-PyA	N1-H1…O2	0.8801(30)	2.1993(25)	3.0579(39)	165.000(203)	1+x, 2+y, z
200.15 K	O4-H4…N2	0.8400(25)	1.7245(32)	2.5612(40)	173.813(198)	-x, 1.5+y, 1.5-z
Fmoc-**DL**-PyA (**P1**)	N1-H1…O2	0.8797(30)	2.2452(26)	3.0928(40)	161.715(204)	1-x, 3-y, 1-z
140.15 K	O4-H4…N2	0.8404(26)	1.8042(30)	2.5942(39)	155.920(207)	1-x, 2-y, 1-z

Table S3. Bond lengths [Å] and angles [°] for Fmoc-**L**-PyA.

Compound	**Bond length**	**Bond angle**	**Compound**	**Bond length**	**Bond angle**
	O1-C14: 1.441(10)	C15-O1-C14: 117.4(7)		C10-C11: 1.369(16)	C13-C12-C11: 119.5(12)
	O1-C15: 1.352(11)	C15-N1-C16: 120.6(8)		C11-C12: 1.405(16)	C8-C13-C1: 110.6(9)
	O2-C15: 1.230(11)	C23-N2-C22: 118.7(9)		C12-C13: 1.398(14)	C8-C13-C12: 119.7(11)
	O3-C18: 1.207(11)	C2-C1-C14: 108.9(8)		C16-C17: 1.533(14)	C12-C13-C1: 129.7(10)
	O4-C18: 1.290(10)	C13-C1-C2: 101.4(8)		C16-C18: 1.508(12)	O1-C14-C1: 110.1(7)
	N1-C15: 1.318(12)	C13-C1-C14: 114.3(8)		C17-C19: 1.515(14)	O2-C15-O1: 121.4(9)
	N1-C16: 1.452(11)	C3-C2-C1: 127.9(10)		C19-C20: 1.403(13)	O2-C15-N1: 125.5(10)
	N2-C22: 1.360(12)	C7-C2-C1: 111.8(10)		C19-C23: 1.388(12)	N1-C15-O1: 113.1(8)
Fmoc-**L**-PyA	N2-C23: 1.345(12)	C7-C2-C3: 120.3(10)	Fmoc-**L**-PyA	C20-C21: 1.388(15)	N1-C16-C17: 112.5(8)
	C1-C2: 1.511(12)	C2-C3-C4: 117.5(12)		C21-C22: 1.382(14)	N1-C16-C18: 110.0(7)
	C1-C13: 1.509(15)	C5-C4-C3: 120.8(13)			C18-C16-C17: 113.3(8)
	C1-C14: 1.531(12)	C6-C5-C4: 120.7(13)			C19-C17-C16: 115.2(7)
	C2-C3: 1.384(14)	C5-C6-C7: 120.3(13)			O3-C18-O4: 124.0(9)
	C2-C7: 1.361(14)	C2-C7-C6: 120.3(11)			O3-C18-C16: 122.9(9)
	C3-C4: 1.431(14)	C2-C7-C8: 108.3(10)			O4-C18-C16: 113.1(8)
	C4-C5: 1.348(18)	C6-C7-C8: 131.3(12)			C20-C19-C17: 123.4(10)
	C5-C6: 1.337(18)	C9-C8-C7: 131.2(12)			C23-C19-C17: 120.9(10)
	C6-C7: 1.399(13)	C9-C8-C13: 120.8(12)			C23-C19-C20: 115.6(10)
	C7-C8: 1.480(15)	C13-C8-C7: 107.9(10)			C21-C20-C19: 121.8(10)
	C8-C9: 1.374(16)	C8-C9-C10: 118.8(13)			C22-C21-C20: 117.9(10)
	C8-C13: 1.393(14)	C11-C10-C9: 122.3(14)			N2-C22-C21: 121.8(11)
	C9-C10: 1.387(16)	C10-C11-C12: 119.0(14)			N2-C23-C19: 123.9(9)

Table S4. Bond lengths [Å] and angles [°] for Fmoc-**D**-PyA.

Compound	**Bond length**	**Bond angle**	**Compound**	**Bond length**	**Bond angle**
	O1-C14: 1.439(4)	C15-O1-C14: 115.3(3)		C10-C11: 1.379(7)	C13-C12-C11: 118.1(5)
	O1-C15: 1.353(5)	C15-N1-C16: 119.4(3)		C11-C12: 1.392(6)	C8-C13-C1: 109.7(4)
	O2-C15: 1.219(5)	C23-N2-C22-118.7(4)		C12-C13: 1.380(6)	C12-C13-C1: 129.1(4)
	O3-C17: 1.207(5)	C13-C1-C2: 102.1(3)		C16-C17: 1.512(5)	C12-C13-C8: 121.2(4)
	O4-C17: 1.304(4)	C14-C1-C2: 108.8(3)		C16-C18:1.534(5)	O1-C14-C1: 109.1(3)
	N1-C15: 1.329(5)	C14-C1-C13: 114.5(3)		C18-C19:1.500(6)	O2-C15-O1: 122.6(4)
	N1-C16: 1.453(5)	C3-C2-C1: 128.8(4)		C19-C20: 1.381(5)	O2-C15-N1: 126.0(4)
	N2-C22: 1.337(5)	C3-C2-C7: 120.9(4)		C19-C23: 1.385(5)	N1-C15-O1: 111.3(3)
Fmoc-**D**-PyA	N2-C23: 1.337(5)	C7-C2-C1: 110.2(4)	Fmoc-**D**-PyA	C20-C21: 1.384(6)	N1-C16-C17: 109.4(3)
	C1-C2: 1.518(5)	C2-C3-C4: 118.7(4)		C21-C22: 1.372(6)	N1-C16-C18: 112.7(3)
	C1-C13: 1.518(6)	C5-C4-C3: 120.2(5)			C17-C16-C18: 113.3(3)

	C1-C14: 1.515(5)	C4-C5-C6: 121.5(5)			O3-C17-O4: 125.2(4)
	C2-C3: 1.378(6)	C5-C6-C7: 118.8(5)			O3-C17-C16: 122.7(3)
	C2-C7: 1.388(6)	C2-C7-C6: 119.8(4)			O4-C17-C16: 112.1(3)
	C3-C4: 1.396(6)	C2-C7-C8: 108.7(4)			C19-C18-C16: 114.5(3)
	C4-C5: 1.369(7)	C6-C7-C8: 131.4(4)			C20-C19-C18: 122.9(4)
	C5-C6: 1.373(7)	C9-C8-C7: 130.7(5)			C20-C19-C23: 116.5(4)
	C6-C7: 1.394(6)	C9-C8-C13: 120.1(5)			C23-C19-C18: 120.6(4)
	C7-C8: 1.456(6)	C13-C8-C7: 109.2(4)			C19-C20-C21: 120.2(4)
	C8-C9: 1.376(6)	C8-C9-C10: 119.2(5)			C22-C21-C20: 119.3(4)
	C8-C13: 1.393(6)	C11-C10-C9: 120.7(5)			N2-C22-C21: 121.5(4)
	C9-C10: 1.381(7)	C10-C11-C12: 120.8(5)			N2-C23-C19: 123.8(4)

Table S5. Bond lengths [Å] and angles [°] for Fmoc-**DL**-PyA (**P1**).

Compound	**Bond length**	**Bond angle**	**Compound**	**Bond length**	**Bond angle**
	O1-C14: 1.425(4)	C15-O1-C14: 115.7(3)		C10-C11: 1.359(7)	C12-C13-C1: 128.3(4)
	O1-C15: 1.348(4)	C15-N1-C16: 118.5(3)		C11-C12: 1.396(7)	C12-C13-C8: 121.1(5)
	O3-C18: 1.196(4)	C22-N2-C2: 117.9(4)		C12-C13: 1.374(6)	O1-C14-C1: 109.2(3)
	O4-C18: 1.306(4)	C13-C1-C14: 112.9(3)		C16-C17: 1.525(5)	O2-C15-O1: 123.7(4)
	N1-C15: 1.332(4)	C13-C1-C23: 101.8(4)		C16-C18: 1.503(5)	O2-C15-N1: 125.2(4)
	N1-C16: 1.441(4)	C14-C1-C23: 107.6(3)		C17-C19: 1.502(5)	N1-C15-O1: 111.1(3)
	N2-C2: 1.334(4)	N2-C2-C19: 124.7(4)		C19-C20: 1.368(5)	N1-C16-C17: 113.1(3)
	N2-C22: 1.333(5)	C23-C3-C4: 118.8(6)		C20-C21: 1.382(5)	N1-C16-C18: 109.8(3)
Fmoc-**DL**-PyA (**P1**)	C1-C13: 1.505(6)	C5-C4-C3: 119.4(7)	Fmoc-**DL**-PyA (**P1**)	C21-C22: 1.377(5)	C18-C16-C17: 113.0(3)
	C1-C14: 1.511(5)	C6-C5-C4: 122.1(7)			C19-C17-C16: 114.6(3)
	C1-C23: 1.521(5)	C5-C6-C7: 118.8(7)			O3-C18-O4: 124.5(4)
	C2-C19: 1.377(5)	C6-C7-C8: 132.1(6)			O3-C18-C16: 124.6(4)
	C3-C4: 1.394(7)	C6-C7-C23: 119.0(6)			O4-C18-C16: 110.9(3)
	C3-C23: 1.364(6)	C23-C7-C8: 108.9(4)			C2-C19-C17: 121.2(4)
	C4-C5: 1.390(8)	C9-C8-C7: 131.4(5)			C20-C19-C2: 116.5(4)
	C5-C6: 1.367(8)	C13-C8-C7: 108.9(5)			C20-C19-C17: 122.3(4)
	C6-C7: 1.395(6)	C13-C8-C9: 119.7(5)			C19-C20-C21: 120.2(4)
	C7-C8: 1.444(7)	C10-C9-C8: 117.9(6)			C22-C21-C20: 119.2(4)
	C7-C23: 1.402(6)	C11-C10-C9: 122.5(6)			N2-C22-C21: 121.6(4)
	C8-C9: 1.410(7)	C10-C11-C12: 120.4(6)			C3-C23-C1: 128.5(5)
	C8-C13: 1.389(6)	C13-C12-C11: 118.3(5)			C3-C23-C7: 121.9(5)
	C9-C10: 1.363(7)	C8-C13-C1: 110.5(4)			C7-C23-C1: 109.4(4)

Table S6. Torsion angles [°] for Fmoc-**L**-PyA.

Compound	**Torsion angle**	**Torsion angle**
	N1-C16-C17-C19: 63.2(11)	C11-C12-C13-C8: 0.4(15)
	N1-C16-C18-O3: 9.7(13)	C13-C1-C2-C3: 178.2(10)
	N1-C16-C18-O4: -172.1(8)	C13-C1-C2-C7: 0.1(10)
	C1-C2-C3-C4: -176.1(9)	C13-C1-C14-O1: 57.8(11)
	C1-C2-C7-C6: 178.0(9)	C13-C8-C9-C10: 0.0(17)
	C1-C2-C7-C8: -1.3(11)	C14-O1-C15-O2: -5.3(15)
	C2-C1-C13-C8: 1.2(10)	C14-O1-C15-N1: 175.5(8)
	C2-C1-C13-C12: 178.7(9)	C14-C1-C2-C3: 57.3(13)
Fmoc-**L**-PyA	C2-C1-C14-O1: 170.4(8)	C14-C1-C2-C7: -120.8(10)
	C2-C3-C4-C5: -1.0(16)	C14-C1-C13-C8: 118.2(9)
	C2-C7-C8-C9: -177.7(12)	C14-C1-C13-C12: -64.3(14)
	C2-C7-C8-C13: 2.1(11)	C15-O1-C14-C1: -142.2(9)
	C3-C2-C7-C6: -0.2(15)	C15-N1-C16-C17: 75.2(11)
	C3-C2-C7-C8: -179.5(9)	C15-N1-C16-C18: -157.5(9)
	C3-C4-C5-C6: -1.4(19)	C16-N1-C15-O1: 176.5(8)
	C4-C5-C6-C7: 3.1(19)	C16-N1-C15-O2: -2.6(16)
	C5-C6-C7-C2: -2.3(16)	C16-C17-C19-C20: -96.7(12)
	C5-C6-C7-C8: 176.8(11)	C16-C17-C19-C23: 82.4(12)
	C6-C7-C8-C9: 3(2)	C17-C16-C18-O3: 136.4(9)
	C6-C7-C8-C13: -177.1(10)	C17-C16-C18-O4: -45.3(11)
	C7-C2-C3-C4: 1.8(14)	C17-C19-C20-C21: -177.8(9)
	C7-C8-C9-C10: 179.8(10)	C17-C19-C23-N2: -178.6(8)
	C7-C8-C13-C1: -2.0(11)	C18-C16-C17-C19: -62.2(12)
	C7-C8-C13-C12: -179.8(9)	C19-C20-C21-C22: -3.3(15)
	C8-C9-C10-C11: -0.5(19)	C20-C19-C23-N2: 0.6(13)
	C9-C8-C13-C1: 177.8(10)	C20-C21-C22-N2: 0.0(15)
	C9-C8-C13-C12: 0.0(15)	C22-N2-C23-C19: -3.8(13)
	C9-C10-C11-C12: 0.8(19)	C23-N2-C22-C21: 3.4(14)
	C10-C11-C12-C13: -0.8(18)	C23-C19-C20-C21: 3.0(15)
	C11-C12-C13-C1: -176.9(11)	

Table S7. Torsion angles [°] for Fmoc-**D**-PyA.

Compound	Torsion angle	Torsion angle
	N1-C16-C17-O3: -11.1(5)	C11-C12-C13-C8: -0.9(6)
	N1-C16-C17-O4: 170.9(3)	C13-C1-C2-C3: -177.4(4)
	N1-C16-C18-C19: -62.3(4)	C13-C1-C2-C7: -2.0(4)
	C1-C2-C3-C4: 174.7(4)	C13-C1-C14-O1: -58.4(5)
	C1-C2-C7-C6: -176.0(4)	C13-C8-C9-C10: -0.6(7)
	C1-C2-C7-C8: 2.5(5)	C14-O1-C15-O2: 4.7(6)
	C2-C1-C13-C8: 0.7(4)	C14-O1-C15-N1: -174.8(3)
	C2-C1-C13-C12: -178.0(4)	C14-C1-C2-C3: -56.0(5)
Fmoc-**D**-PyA	C2-C1-C14-O1: -171.9(3)	C14-C1-C2-C7: 119.5(4)
	C2-C3-C4-C5: 0.3(7)	C14-C1-C13-C8: -116.7(4)
	C2-C7-C8-C9: 176.3(5)	C14-C1-C13-C12: 64.6(6)
	C2-C7-C8-C13: -2.0(5)	C15-O1-C14-C1: 142.9(3)
	C3-C2-C7-C6: -0.2(6)	C15-N1-C16-C17: 156.9(3)
	C3-C2-C7-C8: 178.3(4)	C15-N1-C16-C18: -76.1(4)
	C3-C4-C5-C6: 0.3(7)	C16-N1-C15-O1: -176.3(3)
	C4-C5-C6-C7: -0.8(7)	C16-N1-C15-O2: 4.2(6)
	C5-C6-C7-C2: 0.7(6)	C16-C18-C19-C20: 98.0(5)
	C5-C6-C7-C8: -177.4(4)	C16-C18-C19-C23: -82.4(5)
	C6-C7-C8-C9: -5.4(8)	C17-C16-C18-C19: 62.6(5)
	C6-C7-C8-C13: 176.3(4)	C18-C16-C17-O3: -137.7(4)
	C7-C2-C3-C4: -0.3(6)	C18-C16-C17-O4: 44.3(4)
	C7-C8-C9-C10: -178.8(4)	C18-C19-C20-C21: 178.6(4)
	C7-C8-C13-C1: 0.7(5)	C18-C19-C23-N2: 179.5(3)
	C7-C8-C13-C12: 179.5(4)	C19-C20-C21-C22: 1.1(6)
	C8-C9-C10-C11: 0.2(7)	C20-C19-C23-N2: -0.9(6)
	C9-C8-C13-C1: -177.9(4)	C20-C21-C22-N2: 0.8(6)
	C9-C8-C13-C12: 1.0(6)	C22-N2-C23-C19: 2.8(5)
	C9-C10-C11-C12: -0.2(8)	C23-N2-C22-C21: -2.7(6)
	C10-C11-C12-C13: 0.6(7)	C23-C19-C20-C21: -1.1(6)
	C11-C12-C13-C1: 177.6(4)	

Table S8. Torsion angles [°] for Fmoc-**DL**-PyA (**P1**).

Compound	**Torsion angle**	**Torsion angle**
	N1-C16-C17-C19: 64.6(4)	C13-C1-C23-C3: -178.5(4)
	N1-C16-C18-O3: -0.9(5)	C13-C1-C23-C7: 6.7(5)
	N1-C16-C18-O4: 177.6(3)	C13-C8-C9-C10: 0.0(8)
	N2-C2-C19-C17: -177.8(3)	C14-O1-C15-O2: 3.6(6)
	N2-C2-C19-C20: 1.1(6)	C14-O1-C15-N1: -176.0(3)
	C2-N2-C22-C21: 1.2(6)	C14-C1-C13-C8: 109.1(4)
	C2-C19-C20-C21: -0.1(6)	C14-C1-C13-C12: -67.6(6)
	C3-C4-C5-C6: -0.5(10)	C14-C1-C23-C3: 62.6(6)
Fmoc-**DL**-PyA (**P1**)	C4-C3-C23-C1: -175.8(4)	C14-C1-C23-C7: -112.2(4)
	C4-C3-C23-C7: -1.6(7)	C15-O1-C14-C1: -140.7(4)
	C4-C5-C6-C7: -0.4(10)	C15-N1-C16-C17: 79.2(4)
	C5-C6-C7-C8: -178.2(5)	C15-N1-C16-C18: -153.5(3)
	C5-C6-C7-C23: 0.3(8)	C16-N1-C15-O1: -179.9(3)
	C6-C7-C8-C9: -0.9(9)	C16-N1-C15-O2: 0.4(6)
	C6-C7-C8-C13: -180.0(5)	C16-C17-C19-C2: 91.5(4)
	C6-C7-C23-C1: 175.9(4)	C16-C17-C19-C20: -87.2(5)
	C6-C7-C23-C3: 0.7(7)	C17-C16-C18-O3: 126.4(4)
	C7-C8-C9-C10: -179.0(5)	C17-C16-C18-O4: -55.1(4)
	C7-C8-C13-C1: 3.2(5)	C17-C19-C20-C21: 178.7(3)
	C7-C8-C13-C12: -179.9(4)	C18-C16-C17-C19: -61.0(4)
	C8-C7-C23-C1: -5.2(5)	C19-C20-C21-C22: -0.2(6)
	C8-C7-C23-C3: 179.5(4)	C20-C21-C22-N2: -0.4(6)
	C8-C9-C10-C11: -1.3(9)	C22-N2-C2-C19: -1.6(6)
	C9-C8-C13-C1: -176.1(4)	C23-C1-C13-C8: -5.9(5)
	C9-C8-C13-C12: 0.9(7)	C23-C1-C13-C12: 177.4(4)
	C9-C10-C11-C12: 1.7(10)	C23-C1-C14-O1: 178.3(3)
	C10-C11-C12-C13: -0.7(8)	C23-C3-C4-C5: 1.4(9)
	C11-C12-C13-C1: 175.8(5)	C23-C7-C8-C9: -179.6(5)
	C11-C12-C13-C8: -0.5(7)	C23-C7-C8-C13: 1.3(5)
	C13-C1-C14-O1: 66.7(4)	

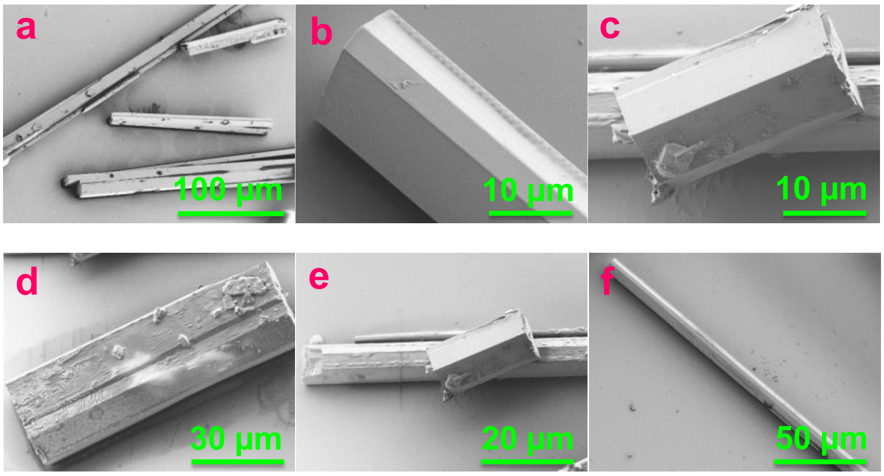

Figure S1. a-f. SEM images of Fmoc-**L**-PyA crystals.

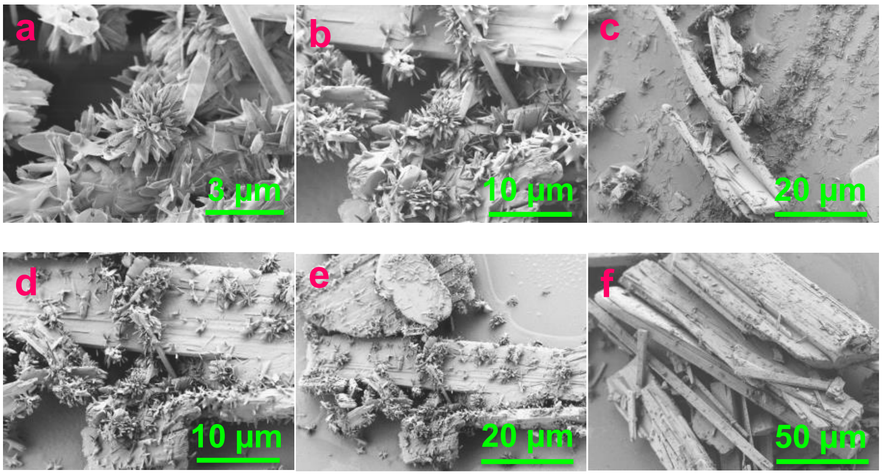

Figure S2. a-f. SEM images of Fmoc-**D**-PyA crystals.

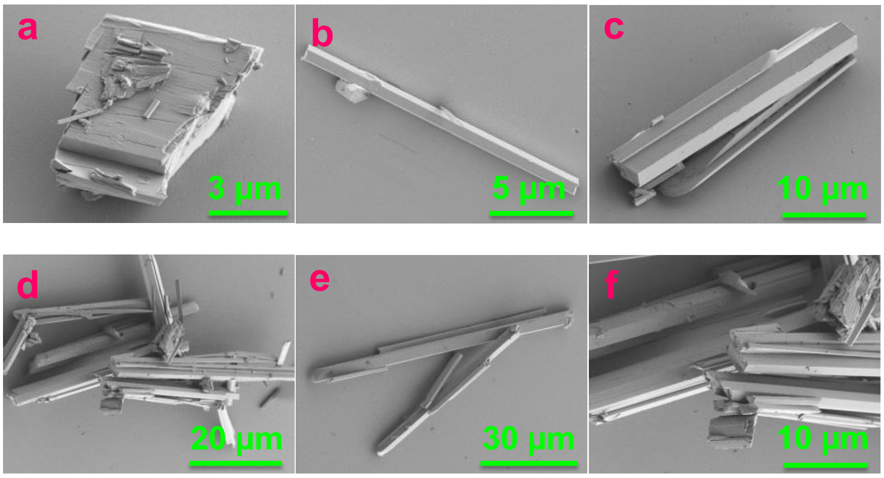

Figure S3. a-f. SEM images of Fmoc-**DL**-PyA (**P1**) crystals.

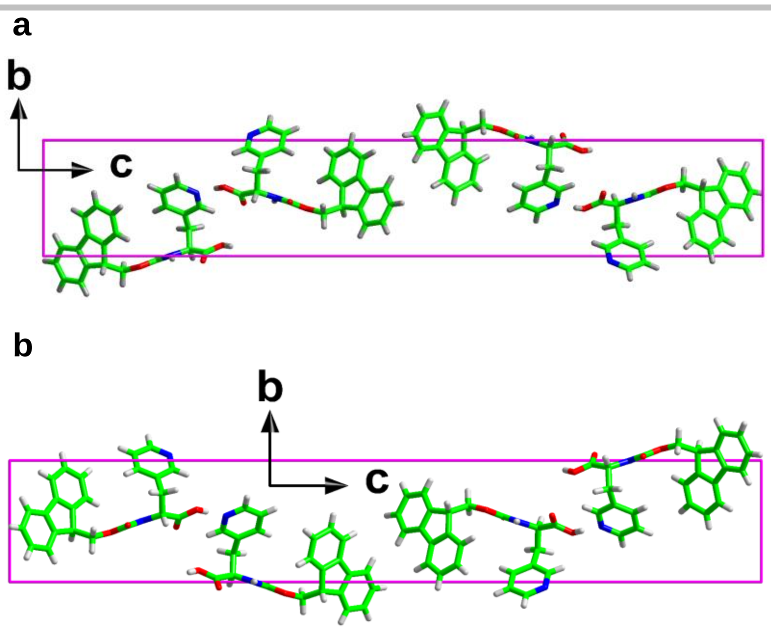

Figure S4. Crystal packing diagram of (a) Fmoc-**L**-PyA and (b) Fmoc-**D**-PyA.

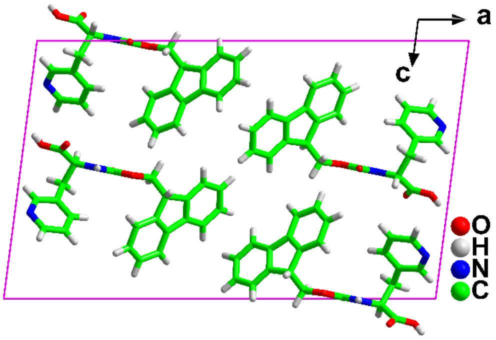

Figure S5. Representation of the crystal packing diagram of Fmoc-**DL**-PyA (**P1**) along the 'b' axis.

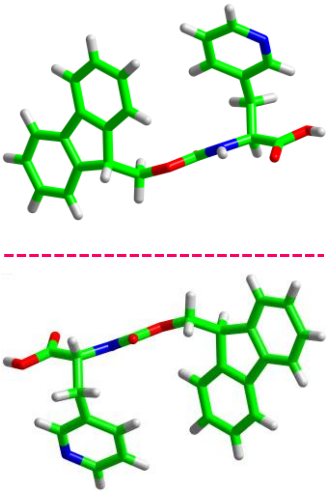

Figure S6. The non-superimposable and mirror-image symmetry of Fmoc-**L**-PyA (top) and Fmoc-**D**-PyA (bottom).

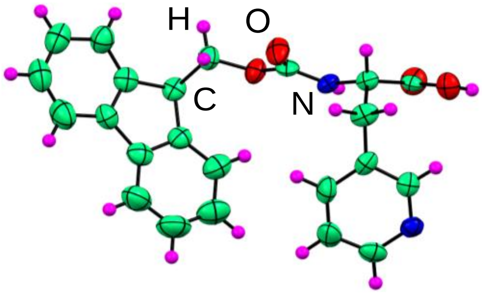

Figure S7. ORTEP diagram of the Fmoc-**L**-PyA asymmetric unit with the thermal ellipsoids set at 50% probability.

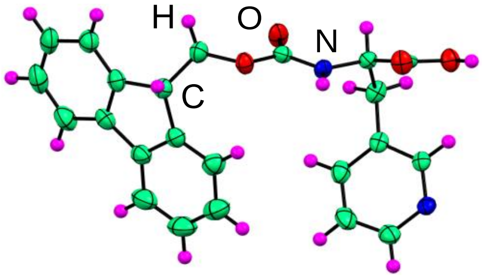

Figure S8. ORTEP diagram of the Fmoc-**D**-PyA asymmetric unit with the thermal ellipsoids set at 50% probability.

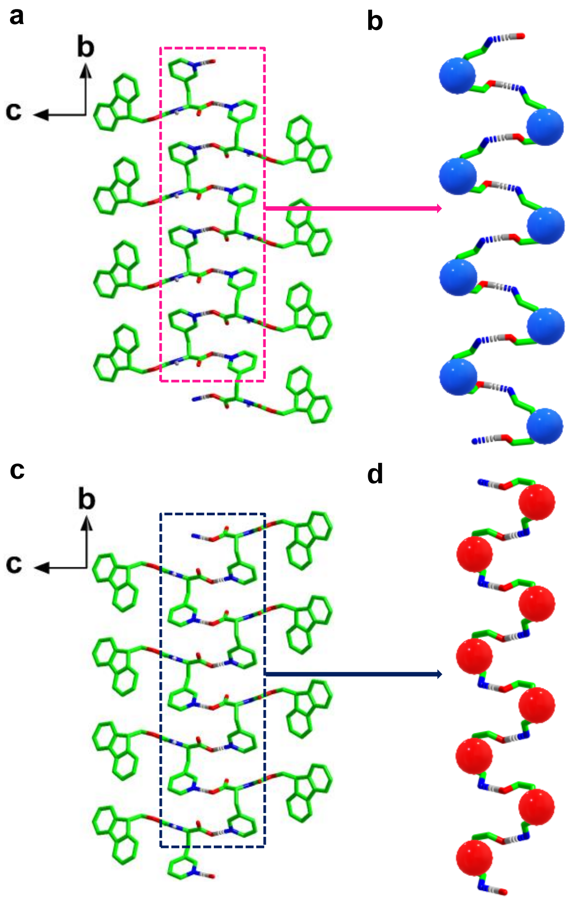

Figure S9. The high-order crystal packing of supramolecular helical organizations formed by (a, b) Fmoc-**L**-PyA and (c, d) Fmoc-**D**-PyA. The highlighted area represents the right and left-handed supramolecular helical assemblies.

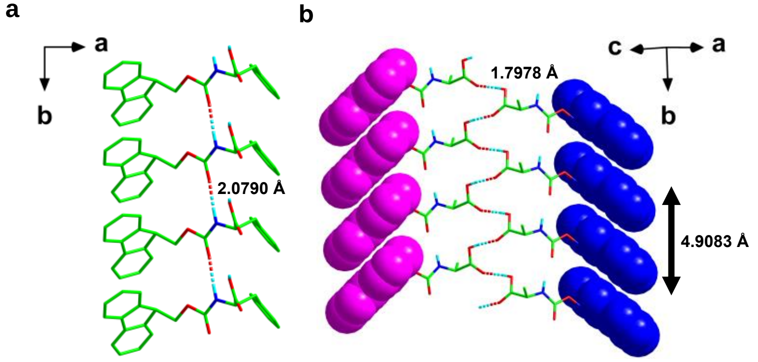

Figure S10. The high-order crystal packing examination of Fmoc-Phe (CCDC: 1060776)[26,27]. (a, b) Inter-amide and inter-carboxylic acid hydrogen-bonded structures displaying parallel and asymmetrical arrangements. The space-filling model is shown to visualize the fluorene segment. The atoms C, H, N and O are coloured green, turquoise, blue and red, respectively.

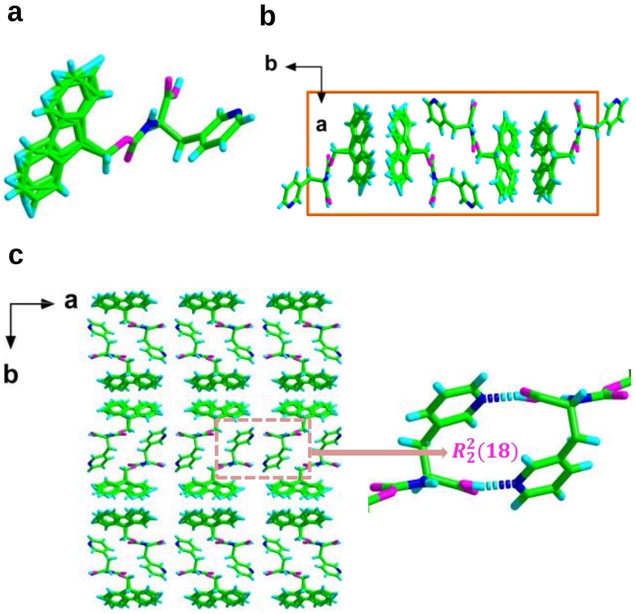

Figure S11. A representation of the **P2** polymorph of the racemic mixture, a. Asymmetric unit. b. Unit-cell crystal packing. c. High-order packing arrangement. The dotted square indicates the H-bonded macrocycle formation mediated by pyridyl nitrogen and carboxylate residue interactions along with the view of a 18-membered ring. The observed **P2** polymorph is similar to **P1**, with only a few small differences in the unit-cell characteristics. The C, H, N, O atoms and the fluorene segment are coloured green, grey, blue, red and magenta, respectively.

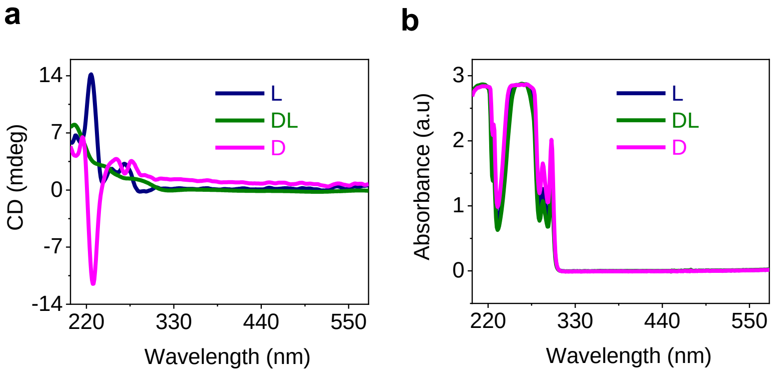

Figure S12. Circular dichroism (a) and absorption spectra (b) of the Fmoc-PyA enantiomers and their conjugated systems.

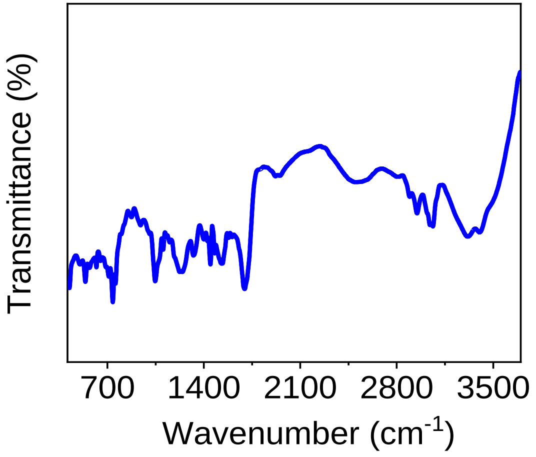

Figure S13. FT-IR spectrum of Fmoc-**L**-PyA.

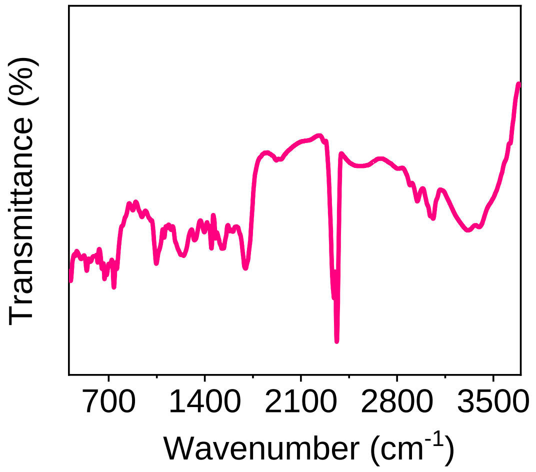

Figure S14. FT-IR spectrum of Fmoc-**D**-PyA.

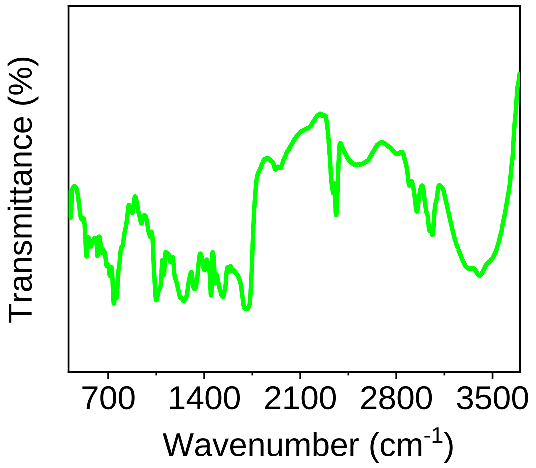

Figure S15. FT-IR spectrum of Fmoc-**DL**-PyA.

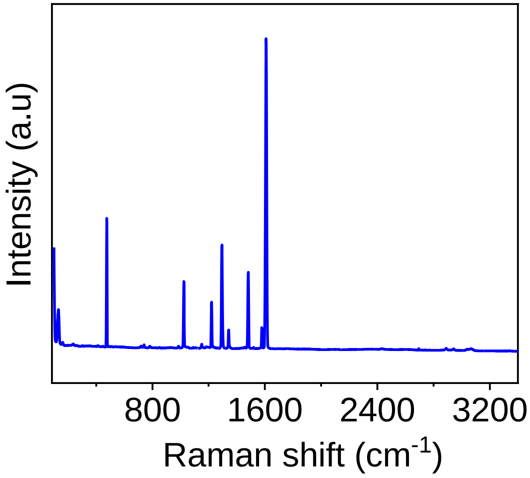

Figure S16. Raman spectrum of Fmoc-**L**-PyA.

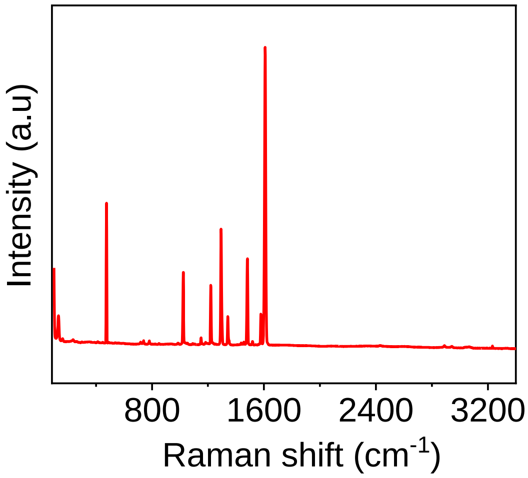

Figure S17. Raman spectrum of Fmoc-**D**-PyA.

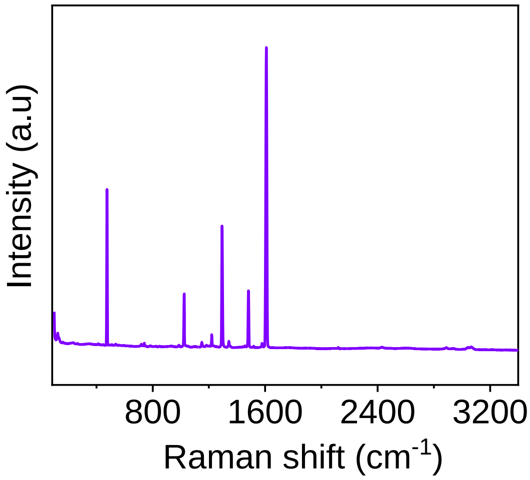

Figure S18. Raman spectrum of Fmoc-**L**-PyA.

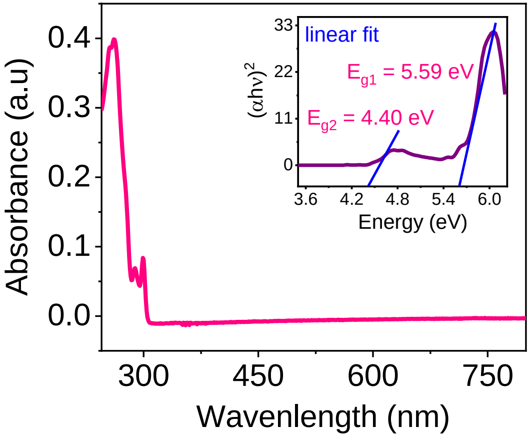

Figure S19. UV-visible absorption spectrum of Fmoc-**L**-PyA. The inset shows the estimated optical band gap from the corresponding Tauc plot.

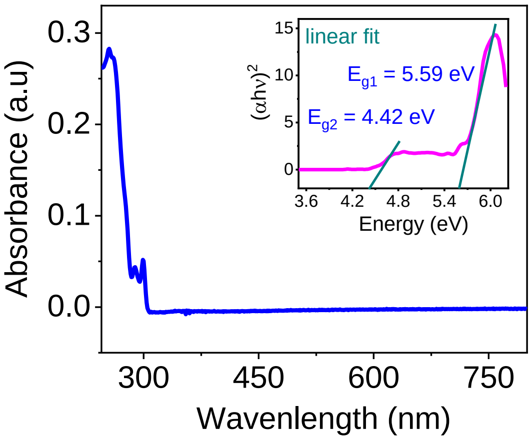

Figure S20. UV-visible absorption spectrum of Fmoc-**D**-PyA. The inset shows the estimated optical band gap from the corresponding Tauc plot.

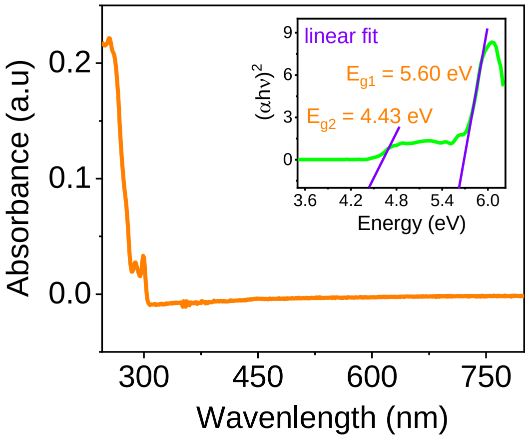

Figure S21. UV-visible absorption spectrum of Fmoc-**DL**-PyA. The inset shows the estimated optical band gap from the corresponding Tauc plot.

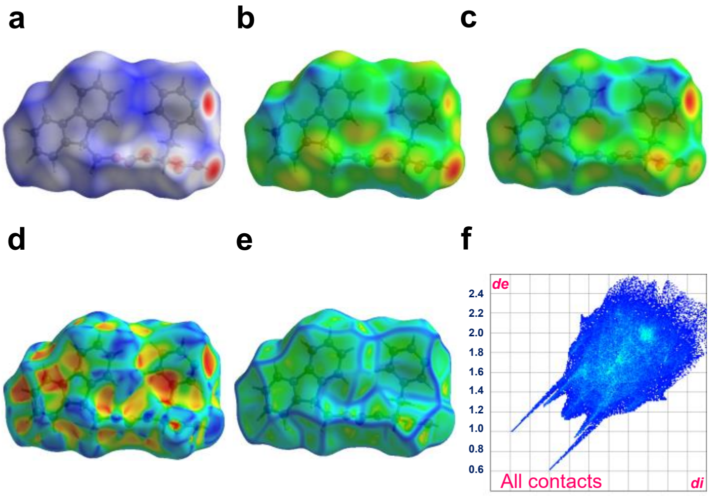

Figure S22. 3D coloured mapping Hirshfeld surface analysis of Fmoc-**L**-PyA showing (a) dnorm, (b) di, (c). de, (d) shape index and (e) curvedness. f. The 2D fingerprint plot (de vs di) of Fmoc-**L**-PyA.

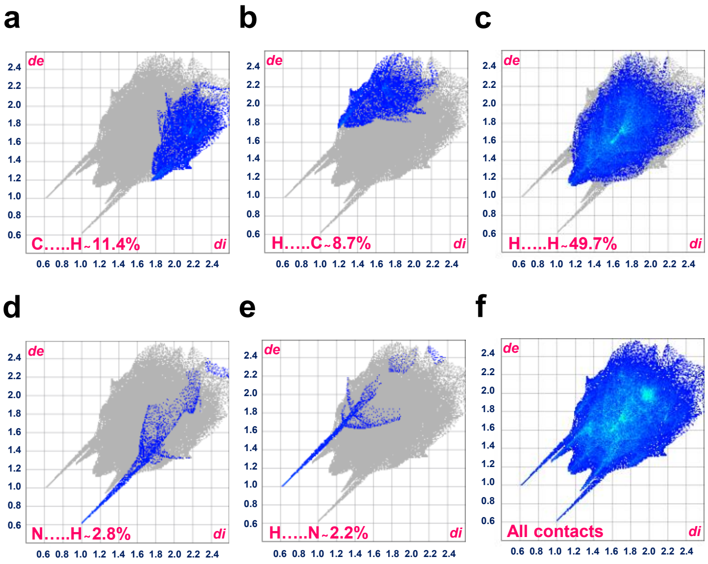

Figure S23. a-f. 2D fingerprint plot (de vs di) of Fmoc-**L**-PyA.

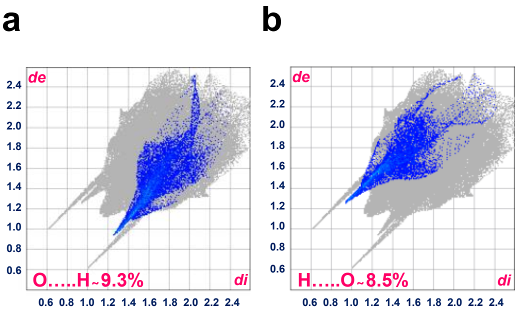

Figure S24. a, b. 2D fingerprint plot (de vs di) of Fmoc-**L**-PyA.

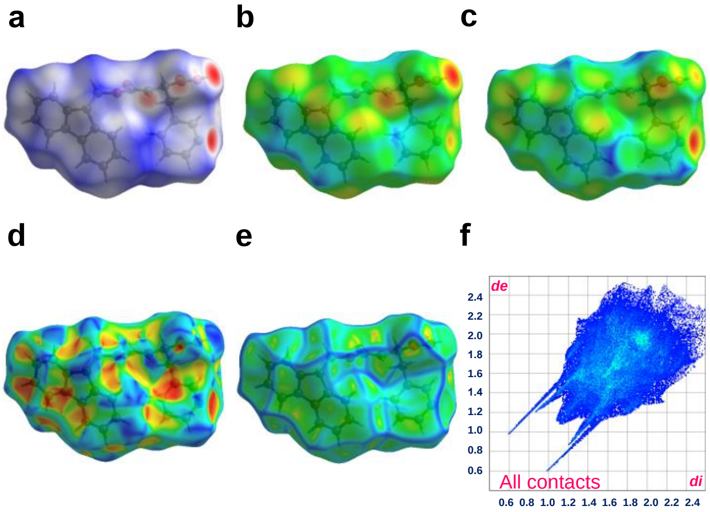

Figure S25. 3D coloured mapping Hirshfeld surface analysis of Fmoc-**D**-PyA showing (a) dnorm, (b) di, (c). de, (d) shape index and (e) curvedness. f. The 2D fingerprint plot (de vs di) of Fmoc-**D**-PyA.

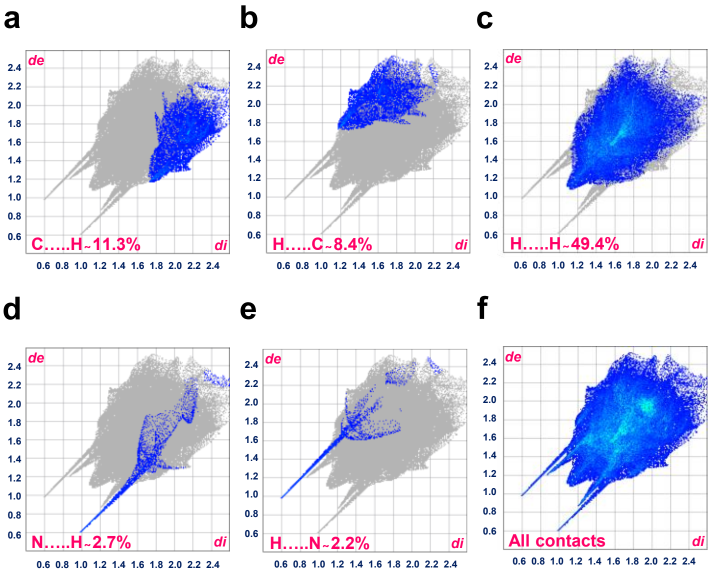

Figure S26. a-f. 2D fingerprint plot (de vs di) of Fmoc-**D**-PyA.

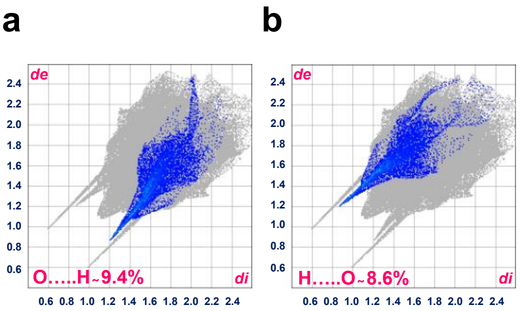

Figure S27. a, b. 2D fingerprint plot (de vs di) of Fmoc-**D**-PyA.

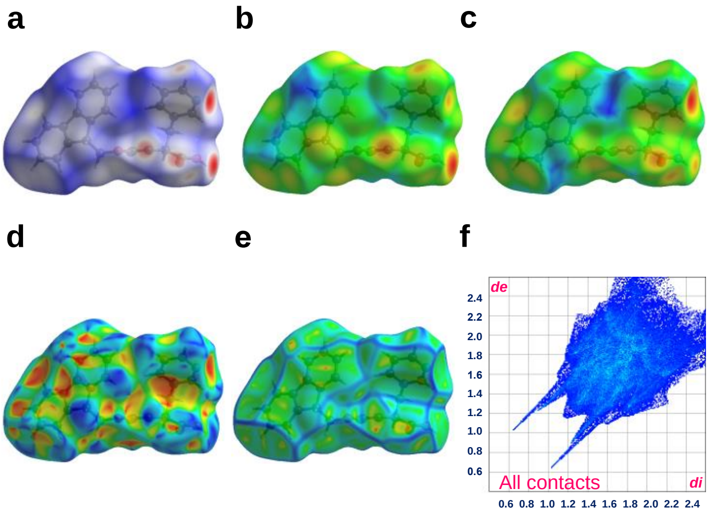

Figure S28. 3D coloured mapping Hirshfeld surface analysis of Fmoc-**DL**-PyA (**P1**) showing (a) dnorm, (b) di, (c). de, (d) shape index and (e) curvedness. f. The 2D fingerprint plot (de vs di) of Fmoc-**DL**-PyA (**P1**).

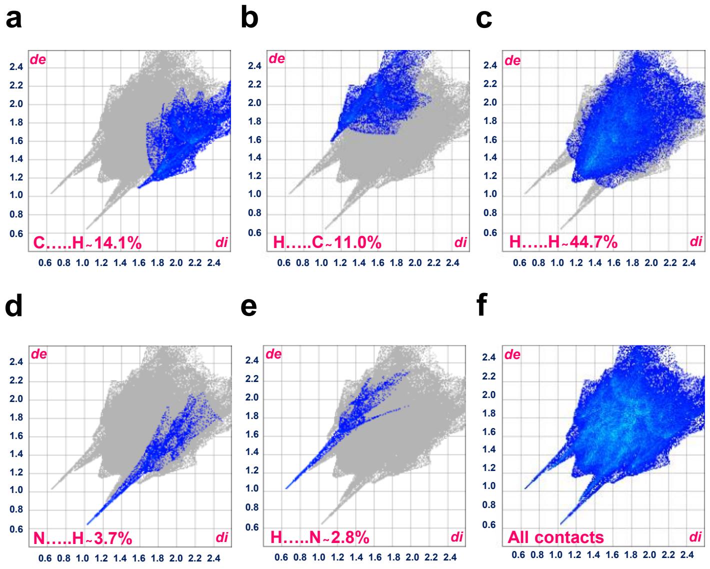

Figure S29. a, f. 2D fingerprint plot (de vs di) of Fmoc-**DL**-PyA (**P1**).

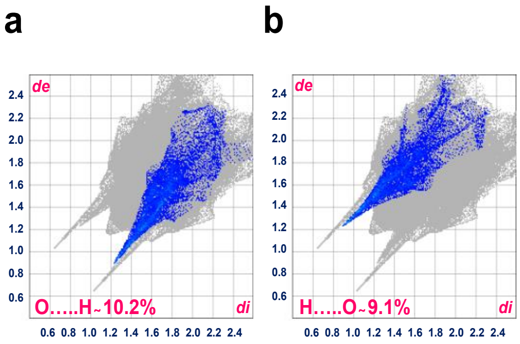

Figure S30. a, b. 2D fingerprint plot (de vs di) of Fmoc-**DL**-PyA (**P1**).

Table S9. Hirshfeld surface analysis of enantiomers and a racemic mixture of Fmoc-PyA.

Compound	**Surface Property**	**Range (Minimum/Maximum)**	**Globularity and Asphericity**	**Surface volume (Å³) and Area (Å²)**
Fmoc-**L**-PyA	di	0.790/3.408		
	de	0.792/3.365		
	dnorm	-0.523/2.357	0.615 and 0.440	1648.82 and 1096.90
	Shape index	-1.000/1.000		
	Curvedness	-4.000/0.400		
Fmoc-**D**-PyA	di	0.790/3.408		
	de	0.792/3.365		
	dnorm	-0.523/2.357	0.615 and 0.440	1648.82 and 1096.90
	Shape index	-1.000/1.000		
	Curvedness	-4.000/0.400		
Fmoc-**DL**-PyA (**P1**)	di	0.790/3.408		
	de	0.792/3.365		
	dnorm	-0.523/2.357	0.615 and 0.440	1648.82 and 1096.90
	Shape index	-1.000/1.000		
	Curvedness	-4.000/0.400		

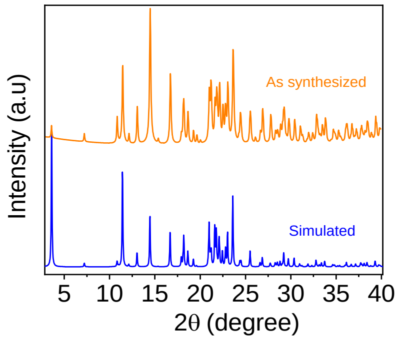

Figure S31. Powder X-ray diffraction pattern of Fmoc-**L**-PyA.

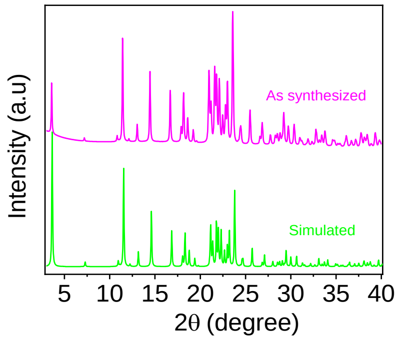

Figure S32. Powder X-ray diffraction pattern of Fmoc-**D**-PyA.

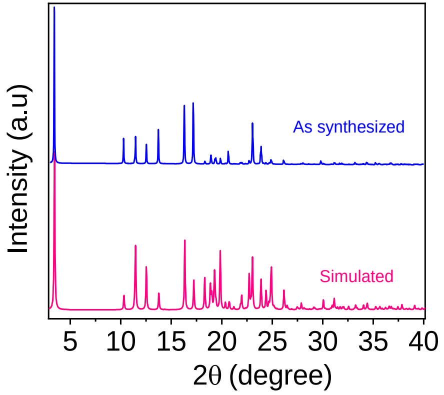

Figure S33. Powder X-ray diffraction pattern of Fmoc-**DL**-PyA (**P1**).

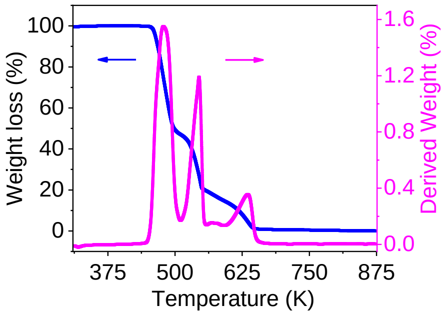

Figure S34. Thermogravimetric examination (blue colour) and the corresponding first derivative plot (magenta colour) of Fmoc-**L**-PyA.

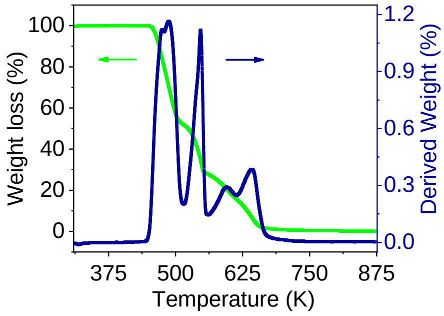

Figure S35. Thermogravimetric examination (green colour) and the corresponding first derivative plot (royal-blue colour) of Fmoc-**D**-PyA.

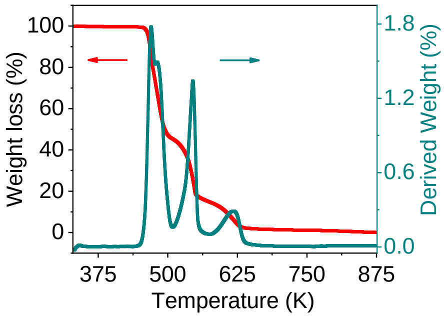

Figure S36. Thermogravimetric examination (red colour) and the corresponding first derivative plot (dark-cyan colour) of Fmoc-**DL**-PyA (**P1**).

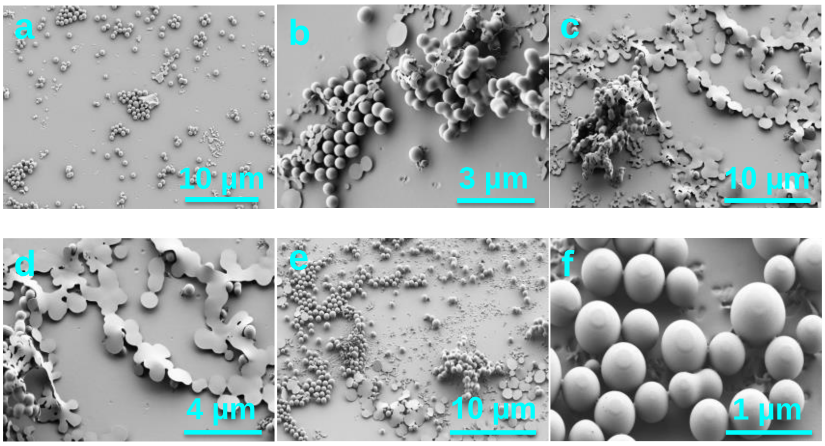

Figure S37. a-f. SEM images of Fmoc-**L**-PyA in MeOH showing sphere-like structural morphologies.

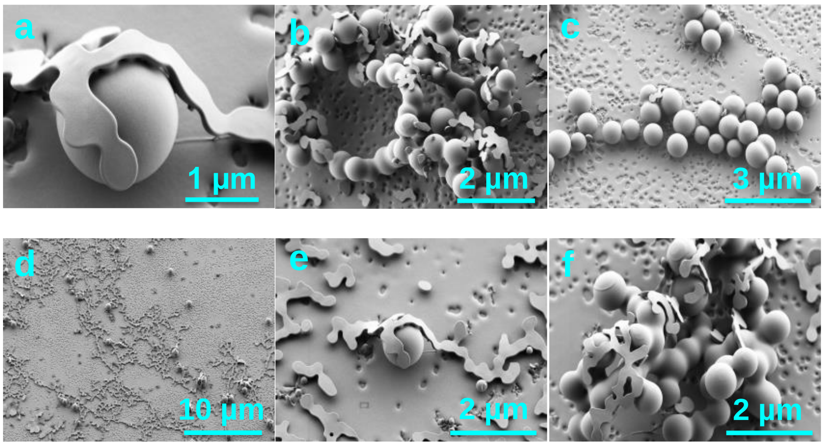

Figure S38. a-f. SEM images of Fmoc-**D**-PyA in MeOH showing sphere-like structural morphologies.

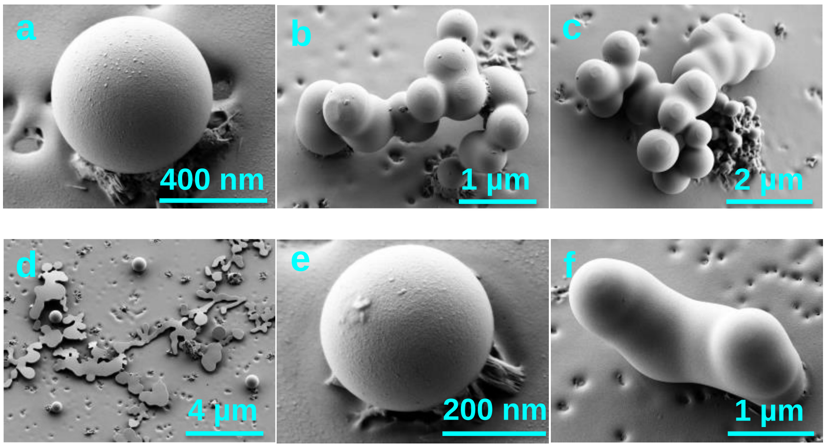

Figure S39. a-f. SEM images of Fmoc-**DL**-Py in MeOH showing sphere-like structural morphologies.

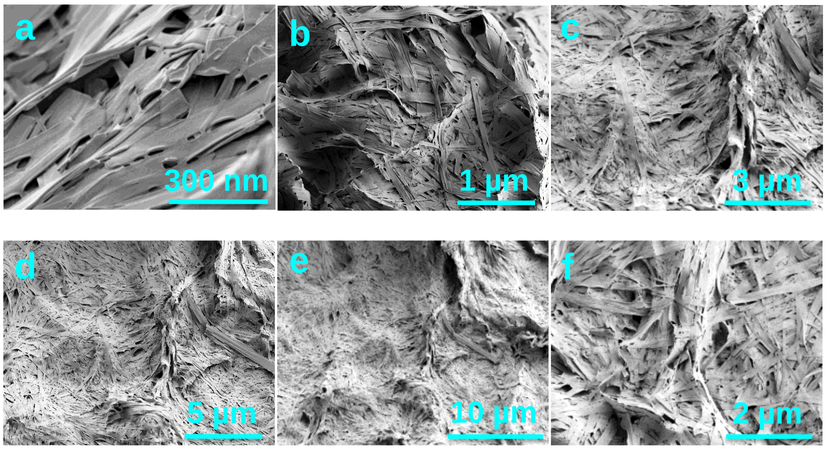

Figure S40. a-f. SEM images of Fmoc-**L**-PyA in MeOH/H_2O showing ribbon-like structural morphologies.

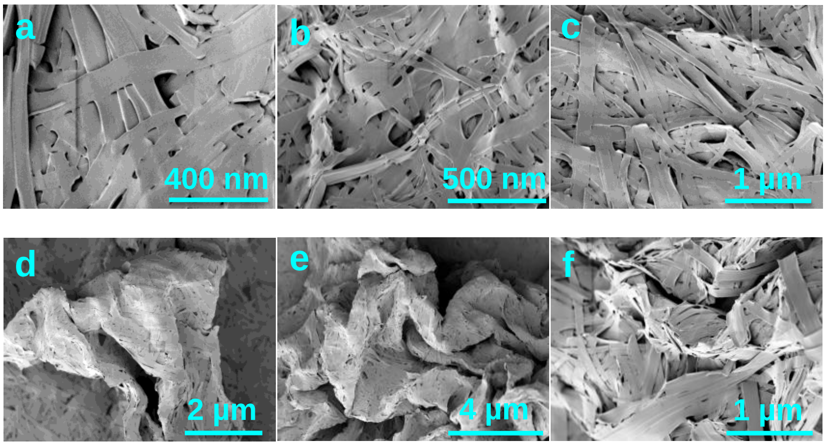

Figure S41. a-f. SEM images of Fmoc-**D**-PyA in MeOH/H_2O showing ribbon-like structural morphologies.

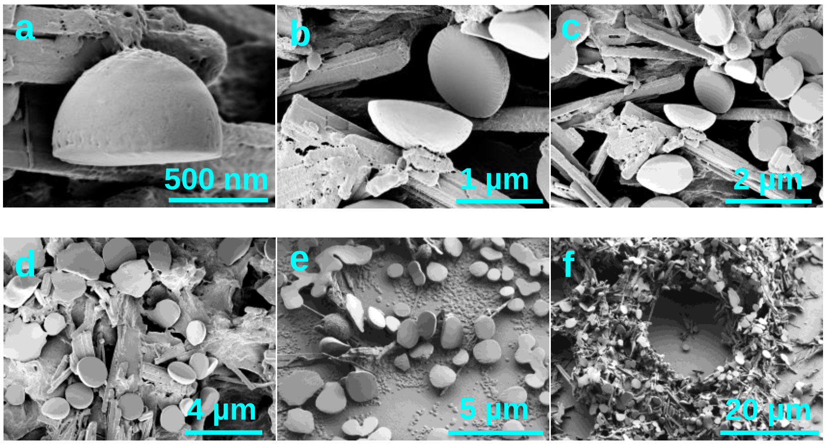

Figure S42. a-f. SEM images of Fmoc-**DL**-PyA in MeOH/H_2O showing micro-sphere and crystal-like structural morphologies.

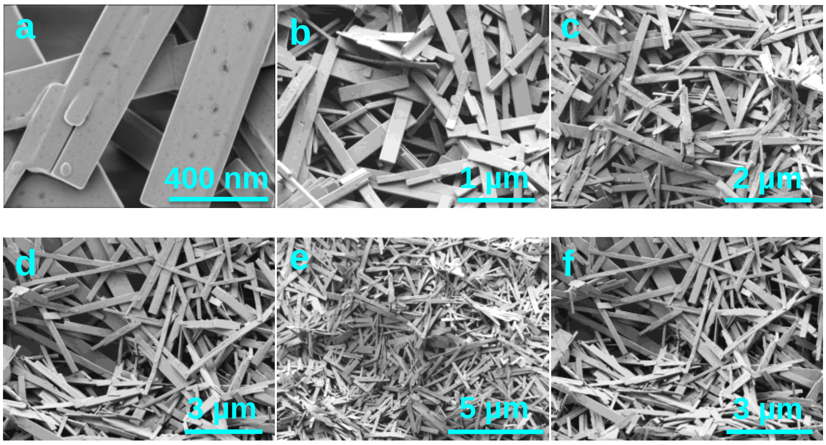

Figure S43. a-f. SEM images of Fmoc-**L**-PyA in DMSO/H_2O showing crystal-like structural morphologies.

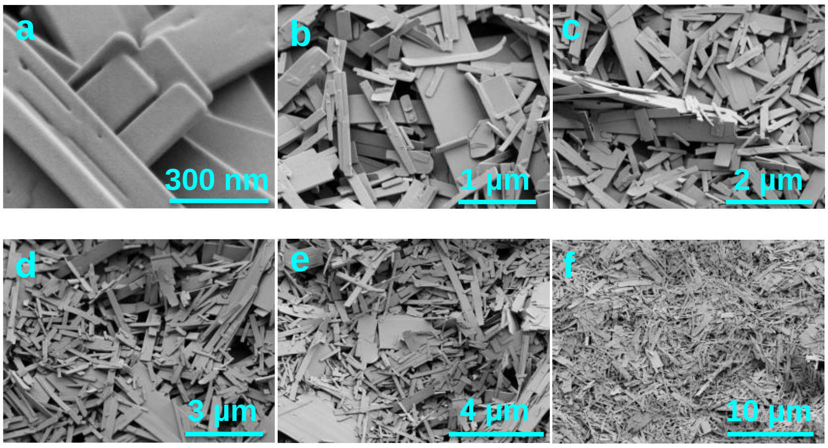

Figure S44. a-f. SEM images of Fmoc-**D**-PyA in DMSO/H_2O showing crystal-like structural morphologies.

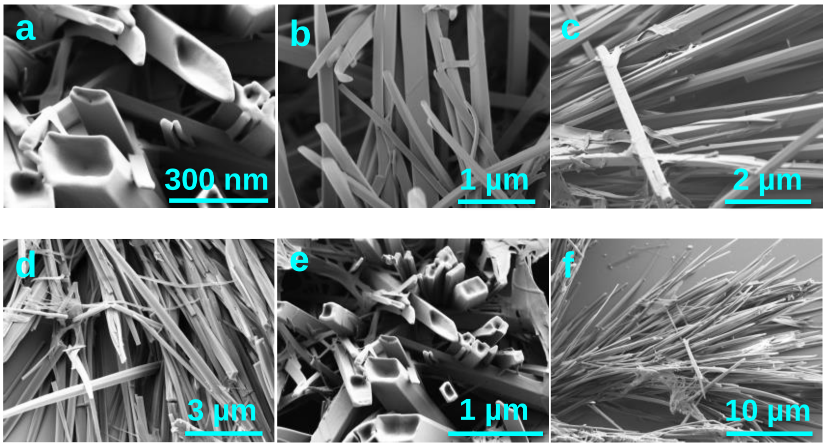

Figure S45. a-f. SEM images of Fmoc-**DL**-PyA in DMSO/H_2O showing crystal-like structural morphologies.

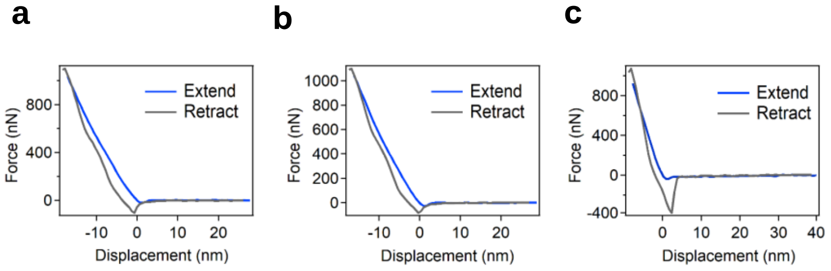

Figure S46. Typical force-displacement traces on the (a) Fmoc-**L**-PyA, (b) Fmoc-**D**-PyA, and (c) Fmoc-**DL**-PyA (**P1**) crystals.

Table S10. DFT-predicted piezoelectric constants of the non-centrosymmetric **L**- and **D**- Fmoc-PyA crystal structures.

	14	**25**	**36**
	Fmoc-**L**-PyA		
$\mathbf{e_{ij}}$	0.034	0.008	0.0013
$\mathbf{d_{ij}}$	11.3	3.3	5.3
$\mathbf{g_{ij}}$	444	113	153
	Fmoc-**D**-PyA		
$\mathbf{e_{ij}}$	0.031	0.003	0.0014
$\mathbf{d_{ij}}$	9.1	0.9	5.3
$\mathbf{g_{ij}}$	349	29	148

Table S11. Comparison of some of the known piezoelectric materials and Fmoc-PyA.

S.No	**Material type**	**Symmetry**	**Direction**	**Piezoelectric coefficient (pC/N)**	**Measurement techniques**	**Ref.**
1	TMAB	$R3m$	Longitudinal (d_{33})	16	Piezometer	28
2	Croconic acid	$Pca2_1$	Longitudinal (d_{33})	15	Piezometer	29
3	Imidazolium periodate	$P2_1$	Longitudinal (d_{33})	4.2	Piezometer	30
4	DPDP·PF_6	Cc	Longitudinal (d_{33})	8	Piezometer	31
5	TPAP·BF_4	Pn	Longitudinal (d_{33})	3	Piezometer	32
6	DPDP·BF_4	Cc	Longitudinal (d_{33})	7	Piezometer	32
7	TIAP·BF_4	$I\text{-}42m$	Longitudinal (d_{33})	3	Piezometer	32
8	TPAP·ClO_4	Pn	Longitudinal (d_{33})	4	Piezometer	32
9	DPDP·ClO_4	Cc	Longitudinal (d_{33})	12	Piezometer	32
10	TIAP·ClO_4	$I\text{-}42m$	Longitudinal (d_{33})	3	Piezometer	32
11	DPDP·IO_4	Cc	Longitudinal (d_{33})	8	Piezometer	32
12	Benzil	$P3_1$	Longitudinal (d_{33})	6	Piezometer	29
13	β-glycine	$P2_1$	Shear response (d_{16})	178	DFT	22
14	γ-glycine	$P3_2$	Longitudinal (d_{33})	9.93	DFT	22
15	L-Alanine	$P2_12_12_1$	Shear response (d_{14})	6	DFT	33
16	L-threonine	$P2_12_12_1$	Shear response (d_{36})	4.90	DFT	33
17	L-tyrosine	$P2_12_12_1$	Shear response (d_{25})	9.73	DFT	33
18	L-glutamine	$P2_12_12_1$	Shear response (d_{36})	11.40	DFT	33

19	L-serine	$P2_12_12_1$	Shear response (d_{14})	4.69	DFT	33
20	Hydroxyproline	$P2_12_12_1$	Shear response (d_{25})	27.75	DFT	33
21	Phe-Phe seed	$P6_1$	Longitudinal (d_{33})	9.4	PFM	34
22	Phe-Phe microrod	$P6_1$	Longitudinal (d_{33})	9.9	PFM	34
23	Phe-Phe microrod (aligned)	$P6_1$	Longitudinal (d_{33})	17.9	PFM	35
24	Cyclo-GW	$P2_1$	Shear response (d_{16}) Shear response (d_{36})	13.8 14.1	DFT DFT	36
25	Fmoc-FF	C2	Shear response (d_{15})	33:7±0:7	PFM	37
26	Pro-Phe-Phe	$P2_1$	Longitudinal (d_{33}) Shear response (d_{22})	2.2 1.9	QFN-AFM measurement DFT	25
27	Hyp-Phe-Phe	$P1$	Longitudinal (d_{33}) Shear response (d_{35})	4.0 27.3	QFN-AFM measurement DFT	25
28	$[Ph_3MeP]_4[Ni(NCS)_6]$	Cc	Longitudinal (d_{33})	8	Piezometer	38
29	$[Ph_2(^iPrNH)_2P]_3[Fe(CN)_6]$	Cc	Longitudinal (d_{33})	7	Piezometer	39
30	$(ATHP)_2PbBr_4$	$Cmc2_1$	Longitudinal (d_{33})	76	PFM	40
31	$(EATMP)PbBr_4$	$C2$	Shear response (d_{22})	16	Piezometer	41
32	Fmoc-**L**-PyA	$P2_12_12_1$	Shear response (d_{14}) Shear response (d_{25}) Shear response (d_{36})	11.3 3.3 5.3	DFT DFT DFT	This work
33	Fmoc-**D**-PyA	$P2_12_12_1$	Shear response (d_{14}) Shear response (d_{25}) Shear response (d_{36})	9.1 0.9 5.3	DFT DFT DFT	This work

Note: TMAB = trimethylamine borane; DPDP·PF_6 = diphenyl diisopropylamino phosphonium hexaflurophosphate; TPAP·BF_4 = triphenyl isopropylaminophosphonium tetrafluoro borate; DPDP·BF_4 = diphenyl diisopropylaminophosphonium tetrafluoro borate; TIAP·BF_4 = tetraisopropylaminophosphonium tetrafluoro borate; TPAP·ClO_4 = triphenyl isopropylaminophosphonium perchlorate; DPDP·ClO_4 = diphenyl diisopropylaminophosphonium perchlorate; TIAP·ClO_4 = Tetraisopropylaminophosphonium perchlorate; DPDP·ClO_4 = diphenyl diisopropylaminophosphonium periodate; Phe-Phe = phenylalanine-phenylalanine; Cyclo-GW = cyclo-glycine-tryptophan; Fmoc-FF = fluorenylmethyloxycarbonyl-phenylalanine-phenylalanine; Pro-Phe-Phe = proline-phenylalanine-phenylalanine; Hyp-Phe-Phe = hydroxyproline-phenylalanine-phenylalanine; $[Ph_3MeP]_4[Ni(NCS)_6]$ = triphenylmethylphosphonium containing hexaisothiocyanatonickelate(II); $[Ph_2(^iPrNH)_2P]_3[Fe(CN)_6]$ = diphenyl diisopropylamino phosphonium containing potassium hexacyanoferrate(II); $(ATHP)_2PbBr_4$; 4-aminotetrahydropyran containing lead bromide(II); $(EATMP)PbBr_4$ = (2-aminoethyl)trimethylphosphonium) containing lead bromide(II).

Table S12. DFT-predicted bulk Young's Modulus and standard deviation, derived from calculated elastic stiffness tensors for the enantiomers and the racemic mixtures.

Crystal	Young's Modulus	Standard Deviation
Fmoc-**L**-PyA	8.4	0.24
Fmoc-**D**-PyA	9.9	0.38
Fmoc-**DL**-PyA (**P1**)	5.8	2.8

References

[1]. G. M. Sheldrick. *Acta Crystallogr. Sect. A* **2008,** *64*, 112–122.
[2]. A. L. Spek. *Acta Crystallogr. Sect. D* **2009**, *65*, 148–155.
[3]. M. J. Turner, J. J. McKinnon, S. K. Wolff, D. J. Grimwood, P. R. Spackman, D. Jayatilaka, M. A. Spackman. *CrystalExplorer 3.1* (2012). The University of Western Australia.
[4]. N. Argaman, G. Makov. *Am. J. Phys.* **2000,** *68,* 69–79.
[5]. J. Hafner. *Comput. Phys. Commun.* **2007,** *177,* 6–13.
[6]. C. Fiolhais, F. Nogueira, M. Marques. A primer in density functional theory. Vol. 620 (Springer Science & Business Media, 2003).
[7]. W. Koch, M. C. Holthausen. *A chemist's guide to density functional theory*. John Wiley & Sons: 2015.
[8]. L. Sass, J. McPhee, C. Schmitke, P. Fisette, D. Grenier. *Multibody Syst. Dyn.* **2004,** *12*, 209–250.

[9]. T. D. Kühne, M. Iannuzzi, M. Del Ben, V. V. Rybkin, P. Seewald, F. Stein, T. Laino, R. Z. Khaliullin, O. Schütt, F. Schiffmann, D. Golze, J. Wilhelm, S. Chulkov, M. H. Bani-Hashemian, V. Weber, U. Borstnik, M. Taillefumier, A. S. Jakobovits, A. Lazzaro, H. Pabst, T. Müller, R. Schade, M. Guidon, S. Andermatt, N. Holmberg, G .K. Schenter, A. Hehn, A. Bussy, F. Belleflamme, G. Tabacchi, A. Glöß, M. Lass, I. Bethune, C. J. Mundy, C. Plessl, M. Watkins, J. VandeVondele, M. Krack, J. Hutter. *J. Chem. Phys.* **2020,** *152,* 194103.

[10]. X. Gonze, F. Jollet, F. Abreu Araujo, D. Adams, B. Amadon, T. Applencourt, C. Audouze, J. M. Beuken, J. Bieder, A. Bokhanchuk, E. Bousquet, F. Bruneval, D. Caliste, M. Côté, F. Dahm, F. Da Pieve, M. Delaveau, M. Di Gennaro, B. Dorado, C. Espejo, G. Geneste, L. Genovese, A. Gerossier, M. Giantomassi, Y. Gillet, D. R. Hamann, L. He, G. Jomard, J. Laflamme Janssen, S. Le Roux, A. Levitt, A. Lherbier, F. Liu, I. Lukacevi˘c, A. Martin, C. Martins, M. J. T. Oliveira, ´S. Poncé, Y. Pouillon, T. Rangel, G. M. Rignanese, A. H. Romero, B. Rousseau, O. Rubel, A. A. Shukri, M. Stankovski, M. Torrent, M. J. Van Setten, B. Van Troeye, M. J. Verstraete, D. Waroquiers, J. Wiktor, B. Xu, A. Zhou, J. W. Zwanziger. *Comput. Phys. Commun.* **2016,** *205,* 106–131.

[11]. S. J. Clark, M. D. Segall, C .J. Pickard, P .J. Hasnip, M. I. J. Probert, K. Refson, M. C. Z. Payne. *Kristallogr.* **2005,** *220,* 567–570.

[12]. J. P. Perdew, J. Chevary, S. Vosko, K. A. Jackson, M. R. Pederson, D. Singh, C. Fiolhais. *Phy. Rev. B* **1992,** *46*, 6671.

[13]. S. Grimme, J. Antony, S. Ehrlich, H. A. Krieg. *J. Chem. Phys.* **2010,** *132,* 154104.

[14]. G. Kresse, D. Joubert. *Phy. Rev. B* **1999,** *59,* 1758.

[15]. X. Wu, D. Vanderbilt, D. Hamann. *Phy. Rev. B* **2005,** *72*, 035105.

[16]. I. Štich, R. Car, M. Parrinello, S. Baroni. *Phy. Rev. B* **1989,** *39*, 4997.

[17]. D. H. Chung, W. R. Buessem. *J. Appl. Phys.,* **1967,** *38,* 2535–2540.

[18]. L. Zuo, M. Humbert, C. Esling. *J. Appl. Crystallogr.,* **1992,** 25*,* 751–755.

[19]. R. Gaillac, P. Pullumbi, F. X. *J. Phys.: Condens. Matter,* **2016,** *28,* 275201.

[20]. K. Momma, F. Izumi. *J. Appl. Crystallogr.,* **2011,** *44,* 1272–1276.

[21]. J. F. Nye. Physical properties of crystals: their representation by tensors and matrices. Oxford university press: 1985.

[22]. S. Guerin, A. Stapleton, D. Chovan, R. Mouras, M. Gleeson, C. McKeown, M. R. Noor, C. Silien, F. M. F. Rhen, A. L. Kholkin, N. Liu, T. Soulimane, S. A. M. Tofail, D. Thompson, *Nat. Mater.* **2017,** *17,* 180–186.

[23]. S. Guerin, S. A. Tofail and D. Thompson. *IEEE Trans. Dielectr. Electr. Insul.,* **2018,** *25,* 803–807.

[24]. W. Ji, B. Xue, S. Bera, S. Guerin, L. J. W. Shimon, Q. Ma, S. A. M. Tofail, D. Thompson, Y. Cao, W. Wang, E. Gazit, *Mater. Today,* **2021,** *42,* 29–40.

[25]. S. Bera, S. Guerin, H. Yuan, J. O. Donnell, N. P. Reynolds, O. Maraba, W. Ji, L. J. W. Shimon, P. A. Cazade, S. A. M. Tofail, D. Thompson, R. Yang, E. Gazit, *Nat. Commun.* **2021,** *12,* 2634.

[26]. E. R. Draper, K. L. Morris, M. A. Little, J. Raeburn, C. Colquhoun, E. R. Cross, T. O. McDonald, L. C. Serpell, D. J. Adams, *CrystEngComm.* **2015,** 17, 8047–8057.

[27]. Z. Wang, A. Hao, P. Xing. *Chin. Chem. Lett.,* **2021,** *32,* 1390–1396.

[28]. Y. Zhang, M. A. Hopkins, D. J. Liptrot, H. Khanbareh, P. Groen, X. Zhou, D. Zhang, Y. Bao, K. Zhou, C. R. Bowen, D. R. Carbery. *Angew. Chem. Int. Ed.* **2020,** *59,* 7808–7812.

[29]. S. Horiuchi, J. Tsutsumi, K. Kobayashi, R. Kumai, S. Ishibashi. *J. Mater. Chem. C,* **2018,** *6,* 4714–4719.

[30]. Y. Zhang, H. Y. Ye, H. L. Cai, D. W. Fu, Q. Ye, W. Zhang, Q. Zhou, J. Wang, G. L. Yuan, R. G. Xiong, *Adv. Mater.* **2014,** *26,* 4515–4520.

[31]. T. Vijayakanth, A. K. Srivastava, F. Ram, P. Kulkarni, K. Shanmuganathan, B. Praveenkumar, R. Boomishankar, *Angew. Chem. Int. Ed.* **2018,** *57,* 9054–9058.

[32]. T. Vijayakanth, F. Ram, B. Praveenkumar, K. Shanmuganathan, R. Boomishankar, *Chem. Mater.* **2019,** *31,* 5964–5972.

[33]. S. Guerin,S. A. M. Tofail, D. Thompson. *Cryst. Growth Des.* **2018,** *18,* 4844−4848.

[34]. V. Nguyen, K. Jenkins, R. Yang. *Nano Energy* **2015,** *17,* 323–329.

[35]. V. Nguyen, R. Zhu, K. Jenkins, R. Yang. *Nat Commun* **2016,** 7, 13566.

[36]. K. Tao, W. Hu, B. Xue, D. Chovan, N. Brown, L. J. W. Shimon, O. Maraba, Y. Cao, S. A. M. Tofail, D. Thompson, J. Li, R. Yang, E. Gazit, *Adv. Mater.* **2019,** *31,* 1807481.

[37]. K. Ryan, J. Beirne, G. Redmond, J. I. Kilpatrick, J. Guyonnet, N. V. Buchete, A. L. Kholkin, B. J. Rodriguez. *ACS Appl. Mater. Interfaces* **2015,** *7,* 12702–12707.

[38]. T. Vijayakanth, F. Ram, B. Praveenkumar, K. Shanmuganathan, R. Boomishankar, *Angew. Chem. Int. Ed.* **2020,** *59,* 10368–10373.

[39]. T. Vijayakanth, S. Sahoo, P. Kothavade, V. B. Sharma, D. Kabra, J. K. Zaręba, K. Shanmuganathan, R. Boomishankar. *Angew. Chem. Int. Ed.* **2023,** *62,* e202214984.

[40]. X. G. Chen, X. J. Song, Z. X. Zhang, P. F. Li, J. Z. Ge, Y. Y. Tang, J. X. Gao, W. Y. Zhang, D. W. Fu, Y. M. You, R. G. Xiong. *J. Am. Chem. Soc.* **2020,** *142,* 1077–1082.

[41]. H. Y. Zhang, Z. X. Zhang, X. G. Chen, X. J. Song, Y. Zhang, R. G. Xiong. *J. Am. Chem. Soc.* **2021,** *143,* 1664–1672.